Impact of Indo-Pacific Feedback Interactions on ENSO Dynamics Diagnosed Using Ensemble Climate Simulations

A. SANTOSO AND M. H. ENGLAND

Climate Change Research Centre, University of New South Wales, Sydney, New South Wales, Australia

W. CAI

CSIRO Marine and Atmospheric Research, Aspendale, Melbourne, Victoria, Australia

ABSTRACT

The impact of Indo-Pacific climate feedback on the dynamics of El Niño–Southern Oscillation (ENSO) is investigated using an ensemble set of Indian Ocean decoupling experiments (DCPL), utilizing a millennial integration of a coupled climate model. It is found that eliminating air–sea interactions over the Indian Ocean results in various degrees of ENSO amplification across DCPL simulations, with a shift in the underlying dynamics toward a more prominent thermocline mode. The DCPL experiments reveal that the net effect of the Indian Ocean in the control runs (CTRL) is a damping of ENSO. The extent of this damping appears to be negatively correlated to the coherence between ENSO and the Indian Ocean dipole (IOD). This type of relationship can arise from the long-lasting ENSO events that the model simulates, such that developing ENSO often coincides with Indian Ocean basin-wide mode (IOBM) anomalies during non-IOD years. As demonstrated via AGCM experiments, the IOBM enhances western Pacific wind anomalies that counteract the ENSO-enhancing winds farther east. In the recharge oscillator framework, this weakens the equatorial Pacific air–sea coupling that governs the ENSO thermocline feedback. Relative to the IOBM, the IOD is more conducive for ENSO growth. The net damping by the Indian Ocean in CTRL is thus dominated by the IOBM effect which is weaker with stronger ENSO–IOD coherence. The stronger ENSO thermocline mode in DCPL is consistent with the absence of any IOBM anomalies. This study supports the notion that the Indian Ocean should be viewed as an integral part of ENSO dynamics.

1. Introduction

El Niño–Southern Oscillation (ENSO), the leading mode of climate variability generated in the tropical Pacific, impacts on various aspects of life worldwide. However, the dynamics behind its evolution are not yet fully understood. It has only recently been realized that apart from the complex governing processes within the Pacific Basin itself, feedback interactions with the Indian Ocean have notable influence on ENSO behavior.

Developing El Niño (La Niña) conditions often induce positive (negative) Indian Ocean dipole (IOD) (Saji et al. 1999) events (Annamalai et al. 2003; Fischer et al. 2005). Anomalous air–sea heat fluxes associated with a maturing El Niño (La Niña) usually promotes a basin-wide warming (cooling) in the Indian Ocean [Klein et al. 1999; Lau and Nath 2003; Du et al. 2009; hereafter referred to as the Indian Ocean basin-wide mode (IOBM)]. These Indian Ocean anomalies, and their interplay with ENSO, influence rainfall over surrounding regions (e.g., Ashok et al. 2001; Watanabe and Jin 2002; Yang et al. 2007; Cai et al. 2011b; Taschetto et al. 2011) and can, in turn, influence ENSO evolution. Kug and Kang (2006) and Kug et al. (2006), for instance, show that easterly wind anomalies induced by Indian Ocean surface warming following the peak of an El Niño facilitate its rapid termination and a faster transition to La Niña.

The IOBM can also occur during the ENSO developing phase. Annamalai et al. (2005) show that from 1950 to 1976, warm IOBM often coincided with developing El Niños during boreal fall. Using atmospheric model experiments, Annamalai et al. (2005) demonstrate that the

Corresponding author address: Agus Santoso, Climate Change Research Centre, University of New South Wales, Sydney, NSW 2052, Australia.
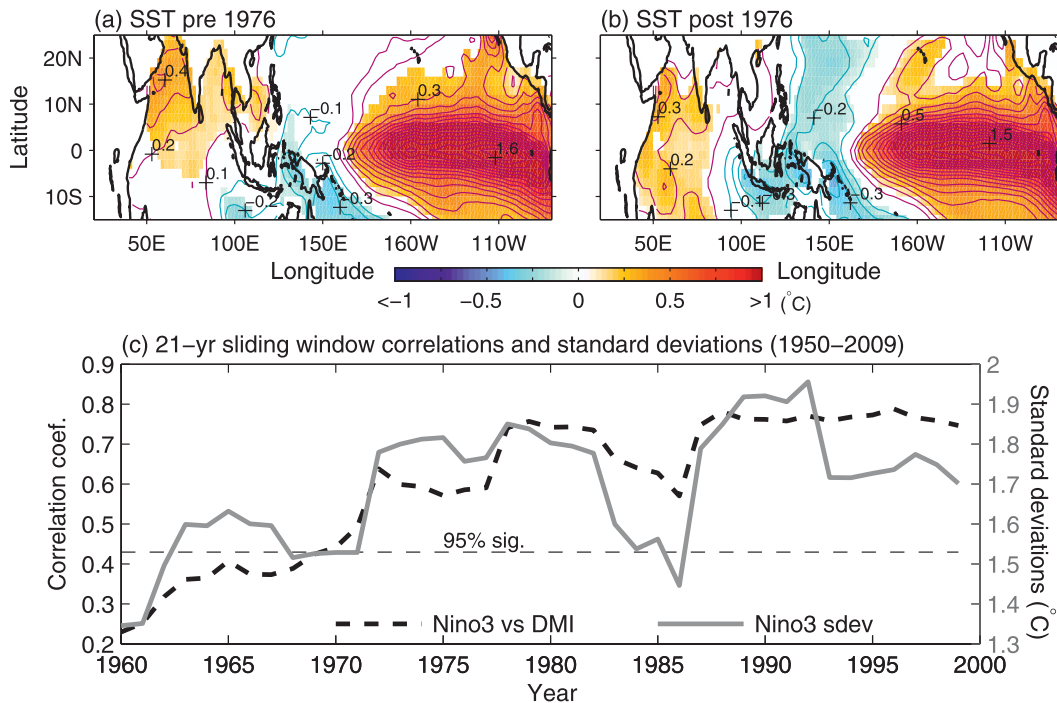E-mail: a.santoso@unsw.edu.au

FIG. 1. El Niño SST composites averaged over September–November for the periods (a) pre-1976 and (b) post-1976, defined as the periods 1950–76 and 1977–2010, respectively, in the NOAA ERSST.v3 reanalysis (color contours). Composites significant above the 90% level are shaded in color. The composites are based on anomalies greater than 0.7 standard deviation above the mean using the Niño-3 index averaged over October–February and detrended over each respective time period. (c) A 21-yr sliding window of correlations between the October–February Niño-3 index and the September–November dipole mode index (thick black dashed line; see Fig. 3 caption for the definition of DMI), and the corresponding 21-yr standard deviation of the Niño-3 index (gray solid line). The horizontal dashed line indicates the 95% cutoff value for the correlations. The years shown along the x axis are at the center of the 21-yr window sliding over 1950–2010.

Indian Ocean basin-wide warming forces easterly wind anomalies over the west-central Pacific, thus weakening the westerly wind anomalies associated with El Niño development. In contrast, after 1976, developing El Niños have been accompanied more frequently by positive IOD events that exert little effect on the Pacific atmospheric circulation, thus allowing El Niño conditions to develop without interruption (Annamalai et al. 2005). As suggested by recent studies, the IOD may even have the potential to enhance ENSO variability (Luo et al. 2010; Izumo et al. 2010). The epochal shift in the ENSO-related SST patterns can be seen in Fig. 1a, in which we have used the National Oceanic and Atmospheric Administration (NOAA) Extended Reconstructed Sea Surface Temperature (ERSST.v3) reanalysis (Smith et al. 2008). Note that using the Hadley Centre SST dataset (HadSST2), which does not involve interpolation nor variance adjustment (Rayner et al. 2006), still produces results similar as to those in Fig. 1 (figure not shown). This suggests that the shift may be an account of reality rather than a result of improvement in the observing

system or a statistical artifact. Although the IOBM pattern during the pre-1976 era does not appear to be as extensive as that shown by Annamalai et al. (2005), the spatial difference between the two periods is clear. This peculiar shift in co-occurrences coincided with a shift in ENSO dynamics, namely, from a predominantly local mode prior to 1976 as characterized by westward-propagating SST anomalies along the equator, toward a thermocline mode post-1976 with stronger El Niños and eastward-propagating anomalies (e.g., Neelin et al. 1998; Fedorov and Philander 2001). This is a possible indication that the Indo-Pacific feedback interactions may be linked to ENSO dynamics. It may not be possible, however, to verify such an epochal link with sufficient confidence using the currently short observational record. Moreover, as noted by Dommenget et al. (2006), it is difficult to verify the impact of the Indian Ocean on ENSO using statistical analysis alone, due to the strong ENSO influence on the Indian Ocean. As illustrated in Fig. 1b, the correlation between ENSO and IOD gradually increases over time, along with increasing magnitude

of ENSO variability in recent decades. Such synchronous evolution is expected, given IOD events can be triggered by ENSO. In this present study, we demonstrate that Indian Ocean feedback processes can in turn influence ENSO dynamics.

The role of the Indian Ocean on ENSO has been inferred in a few studies via eliminating air–sea interactions in the Indian Ocean in coupled general circulation models (CGCMs). Yu et al. (2002), Wu and Kirtman (2004), and Yu et al. (2009) found that decoupling the Indian Ocean weakened ENSO variability in their models. Dommenget et al. (2006), on the other hand, found an opposite result. The former studies were based on a single and relatively short experimental run on the order of 50 yr, whereas the latter of a much longer integration of 500 yr. It remains unclear whether these discrepancies are due to intrinsic model biases, or to differences in integration times and/or a limited number of experimental samples. This present study aims to demonstrate the possible link between the Indo-Pacific climate interactions and ENSO dynamics by conducting ensemble sets of 100-yr-long Indian Ocean decoupling experiments utilizing a coupled climate model. While the use of ensemble experiments is necessary to achieve better statistical significance, it was also motivated by the previous conflicting results.

The rest of the paper is organized as follows. In section 2, we provide an overview of the climate model and experimental design. The model's ability in simulating the Indo-Pacific variability is assessed in section 3. Section 4 discusses the response of the model ENSO dynamics to a decoupled Indian Ocean. We provide further diagnosis of the Indo-Pacific coupling in section 5. The study is concluded in section 6 with further discussions.

2. The climate model and experimental design

This study employs the Commonwealth Scientific and Industrial Research Organisation Mark version 3L (CSIRO Mk3L) model. CSIRO Mk3L is a comprehensive CGCM designed specifically for millennial-scale climate simulation (Phipps 2010). The AGCM resolution is $5.6°$ (zonal) $\times 3.2°$ (meridional), with 18 vertical levels. The OGCM resolution is $2.8° \times 1.6°$, with 21 vertical levels of increasing thickness with depth. The version used in this study is an update to that used by Santoso et al. (2011) to study ENSO processes in relation with the Indonesian Throughflow. Of particular relevance to the present study is that the ENSO period and simulations of the Indian Ocean variability are now better compared to what is observed, partly as a result of an updated configuration of the Indonesian archipelago. As will be shown in section 3, the CSIRO Mk3L does

a reasonable job in simulating the large-scale features of Indo-Pacific climate variability, particularly given the coarse model resolution.

To obtain the control coupled simulation, the OGCM was first spun up for 7000 yr by which the ocean surface variables were used to spin up the AGCM for 100 yr. The AGCM and OGCM were then coupled, with constant flux adjustment terms applied to minimize drift and maintain realistic seasonal climatology (see Santoso et al. 2011 for further details). The coupled model was integrated for 1500 yr, with CO_2 concentration fixed at 280 ppm. The last 1100 yr of this control simulation (CTRL hereafter), which exhibit a stable climate, were used to perform 11 decoupling experiments (DCPL hereafter), each of 100 yr. Specifically, for each consecutive epoch of 100 yr spanning the entire 1100 yr, the full coupled model is run as CTRL, except the model's long-term climatological SSTs were prescribed over the Indian Ocean domain (gray region in Fig. 2a). In this way, the atmosphere does not "feel" any anomalous Indian Ocean SSTs over the decoupled region, so feedback from the Indian Ocean is absent in the DCPL runs. Thus, there are clearly no modes of Indian Ocean variability that can influence the Pacific climate in experiment DCPL.

It is necessary to note that each of the 11 DCPL runs corresponds to the same initial conditions as the respective epoch in CTRL, thus allowing a direct comparison between the pair. The purpose of using 100-yr-long datasets for each epoch is to ensure that the simulated ENSO-like variability in both CTRL and DCPL are fully sampled, given the near-decadal ENSO period, particularly in DCPL (see the appendix for details). Moreover, the purpose in utilizing the entire 1100-yr dataset and simply partitioning it equally into eleven 100-yr chunks is to capture varying climate states and thus Indo-Pacific feedback, without having prior expectation of certain feedback mechanisms that could affect ENSO dynamics. As demonstrated in section 5, this ensemble approach, with the aid of the decoupling experiment, allows us to diagnose a link between ENSO dynamics and Indo-Pacific feedback interactions.

3. Validation of simulated Indo-Pacific variability

At present, simulating ENSO and Indian Ocean variability in CGCMs remains a challenge (Guilyardi et al. 2009; Saji et al. 2006). The majority of climate models submitted to the Intergovernmental Panel on Climate Change (IPCC) Fourth Assessment Report (AR4) simulate IOD-like variability with various degrees of realism (Saji et al. 2006; Liu et al. 2011). For example, as shown by Saji et al. (2006), a number of these models fail
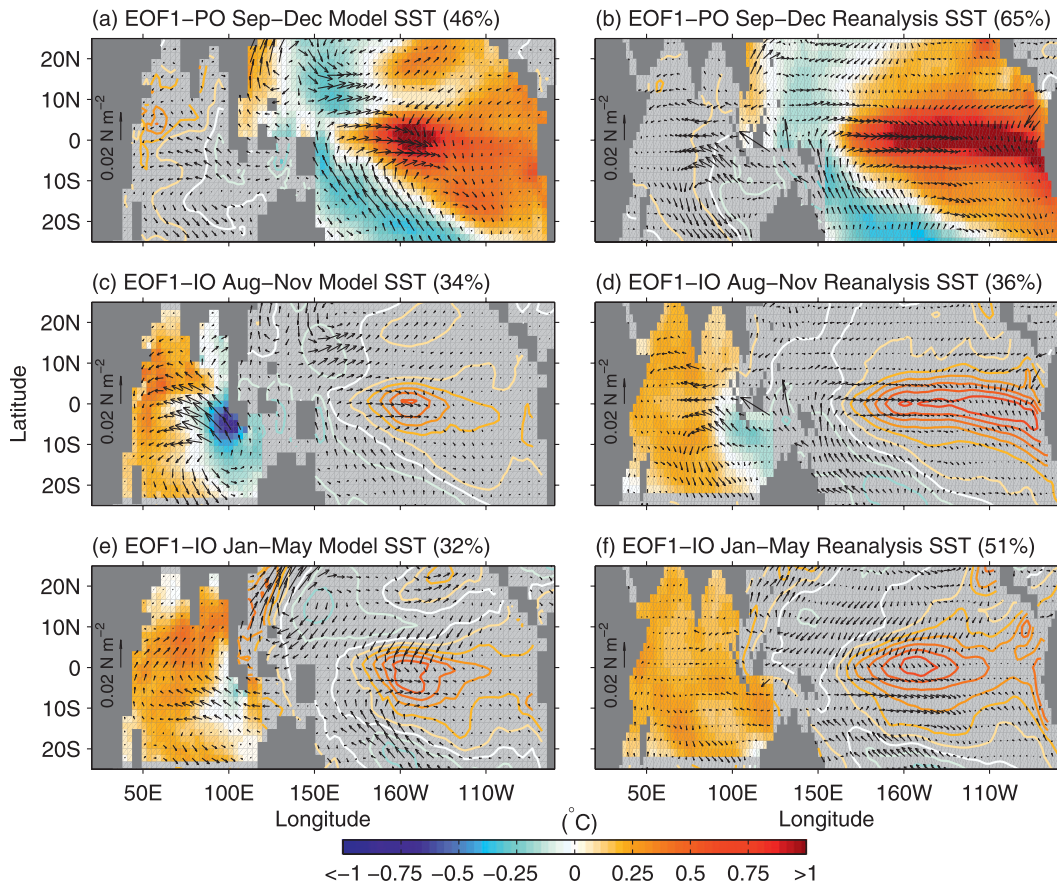
FIG. 2. EOF analysis of SST presented as regression maps for (a),(c),(e) the model and (b),(d),(f) the NOAA ERSST.v3 reanalysis for 1950–2010 over the color-shaded domains of the (a),(b) Pacific and (c)–(f) Indian Oceans. The SST regressions outside the EOF domains are shown in colored contours. The Pacific EOFs (a) and (b) are computed for SSTs averaged over September–December, representing typical El Niño conditions. The IOD in (c) and (d) is revealed using SSTs averaged over August–November, and the IOBM in (e) and (f) is for SSTs averaged over January–May. The vectors represent regressions of surface wind stresses. National Centers for Environmental Prediction–National Center for Atmospheric Research (NCEP–NCAR) reanalysis wind stresses over 1970–2006 are used for (b),(d), and (f). The model EOF analysis is based on 500 yr of data.

to correctly simulate the IOBM as a response to ENSO, as attributed to the too small amplitude and/or un-realistic seasonality of the simulated ENSO variability. The CSIRO Mk3L model performs fairly well in these aspects, capturing ENSO-, IOD-, and IOBM-like vari-abilities with spatial patterns, seasonality, and temporal characteristics that compare reasonably well to the ob-served (Figs. 2 and 3). Biases are nonetheless apparent. For ENSO, the core of its SST anomalies is notably lo-cated farther west than observed. This is a systematic bias associated with the equatorial Pacific SST that is too cold, with overly strong trade winds, and too little pre-cipitation over the warm pool region (Fig. 4). This so-called cold-tongue bias is inherent across many IPCC-class climate models (Cai et al. 2009; Luo et al. 2005). Fur-thermore, the ENSO peaks in boreal fall instead of

winter, with weaker magnitude and longer period than observed (Figs. 3a,d). This could be expected given the coarse resolution, which renders more diffused ther-mocline structures, and which can hardly resolve the oceanic equatorial waveguide, and leads to more slug-gish currents as a consequence of the high viscosity re-quired to maintain numerical stability. These are expected to slow down the propagation of ENSO anomalies and, thus, increase the ENSO period.

The model ENSO can generate IOD events in boreal fall, as evidenced by a positive ENSO–IOD correlation (≈0.4; Fig. 3h) associated with the interannual spectral peaks of the IOD coinciding with those of ENSO (Fig. 3b). While statistically significant, the correlation how-ever is not very high, indicating that IOD events in the model can also arise entirely independently of ENSO.
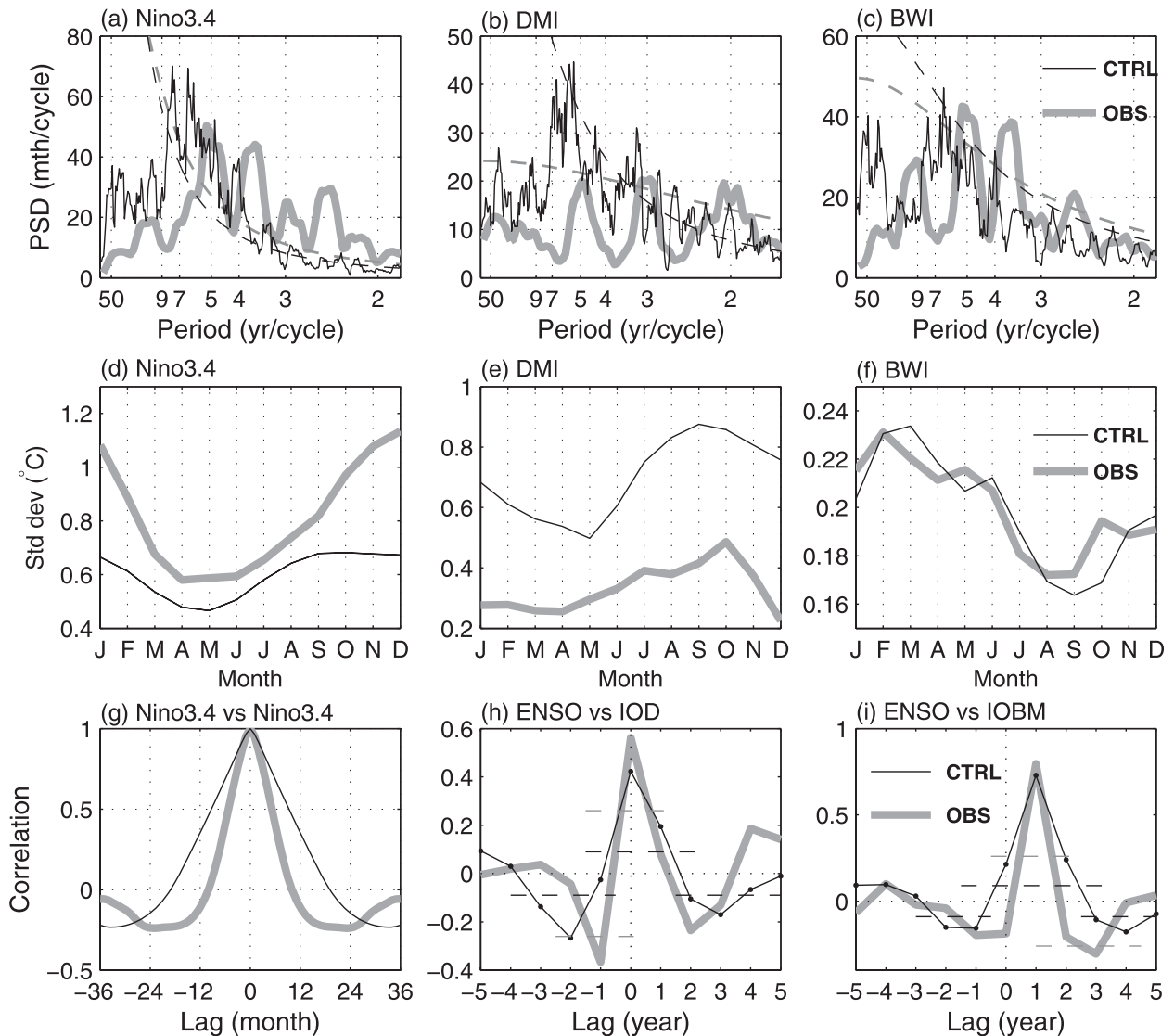
FIG. 3. Power spectral densities (PSDs) of the following indices: (a) Niño-3.4 (5°S–5°N, 170°–120°W), (b) dipole mode index (DMI), and (c) basin-wide index (BWI) in CTRL (black) and 1950–2010 NOAA ERSST v3 (thick gray). The DMI is derived from the difference between SST anomalies averaged over the western (10°S–10°N, 50°–70°E) and eastern (10°S–0°, 90°–110°E) regions of the Indian Ocean (Saji et al. 1999). The BWI is a time series of the basin-wide average SSTs over 20°S–20°N, 40°–100°E (Saji et al. 2006). The analysis is based on monthly time series with the seasonal mean removed (61 yr for reanalysis and 500 yr for the model). For easier comparison of spectral structures, the indices were standardized prior to computing the spectra via the multitaper spectral method (Percival and Walden 1993). Zero padding was applied to the reanalysis time series to enhance frequency resolution. The corresponding dashed curves indicate the 95% significance level of the red noise spectra. (d)–(f) Standard deviations of the indices at each calendar month. Lag-correlation analysis for (g) Niño-3.4 vs Niño-3.4, (h) ENSO vs IOD, and (i) ENSO vs IOBM. In (h) and (i), the time series correspond to the first principal component of the EOF analysis shown in Fig. 2; the 95% significance level is indicated by the corresponding dashed lines for both the model and the reanalysis. Positive (negative) time lags indicate ENSO leading (lagging) IOD and IOBM.

By switching off air–sea coupling over the Pacific, we find that IOD variability is largely retained (figure not shown). This result is consistent with that of Behera et al. (2006) and Fischer et al. (2005), suggesting that the IOD arises from a Bjerknes feedback that can be excited by processes other than ENSO. The simulated IOD appears to be stronger when compared with observations over the last 60 yr (Figs. 2c and 3e) but is similar to those simulated by the majority of the IPCC AR4 models (Cai et al. 2009, their Fig. 10). The stronger and more ENSO-independent IOD than is seen in the observations is consistent with the positive IOD-like
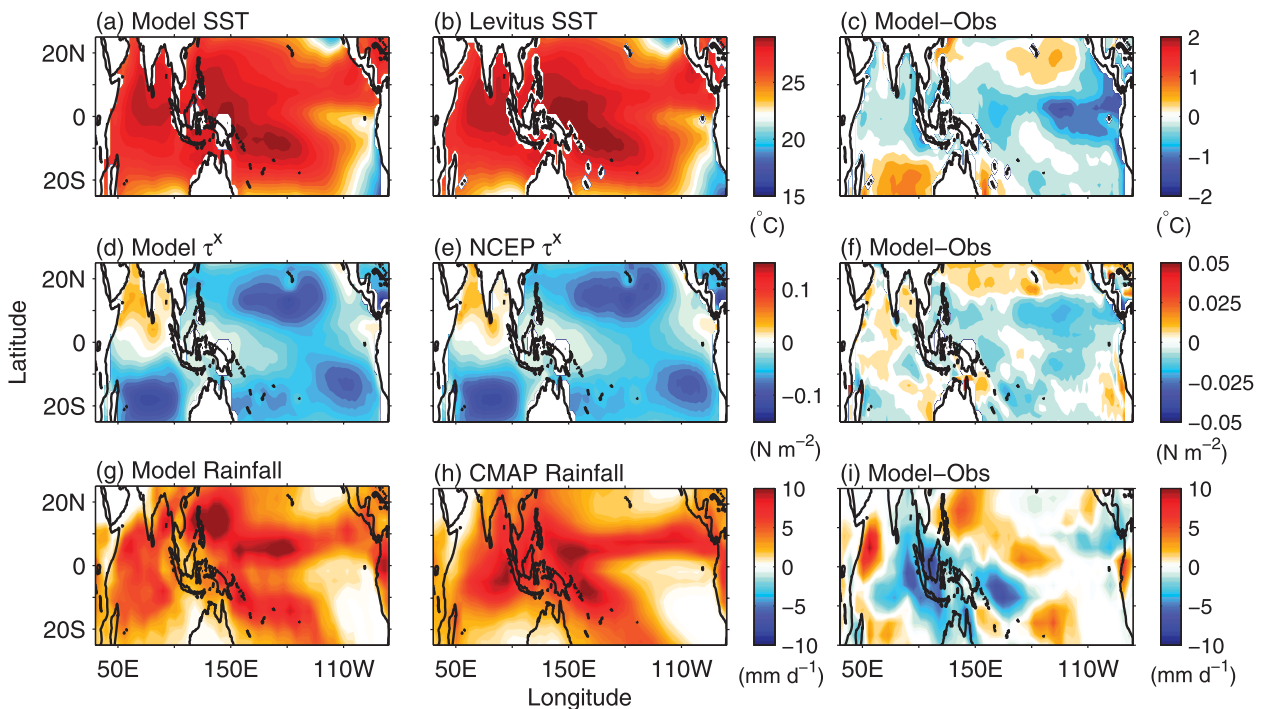
FIG. 4. Comparison of climatological fields in (a),(d),(g) the model to (b),(e),(h) the observations for (a)–(c) SST, (d)–(f) zonal wind stress, and (g)–(i) rainfall. (c),(f),(i) The differences between the left and middle columns. The observational data are the Levitus climatology for SST, NCEP–NCAR reanalysis data for wind stress, and Climate Prediction Center (CPC) Merged Analysis of Precipitation for rainfall.

climatological bias in the model, marked by anomalously cold SST, stronger trade winds, and low rainfall over the eastern Indian Ocean (Fig. 4). This is associated with a more shoaled thermocline in that region (figure not shown), which spuriously enhances air–sea coupling, and thus SST anomalies can be more easily initiated (Saji et al. 2006; Santoso et al. 2010; Liu et al. 2011).

The IOBM usually follows the peak of ENSO in the model as in the real system, as noted by the high positive correlation in Fig. 3i, which reveals a lag correlation between the Niño-3.4 time series averaged over September–December and a basin-wide mode index averaged over January–May. Most of the spectral peaks of the IOBM time series correspond with those of ENSO, except on multidecadal time scales, indicating that the IOBM is largely a response to ENSO in the model and observations. The seasonal phase locking of the model's IOBM is consistent with that observed (Fig. 3f). The spatial pattern of the warm (cool) IOBM, however, includes slight cooling (warming) over the southeastern Indian Ocean (Figs. 2e,f). This bias is due to the persistence of the model's eastern pole of the IOD, which is related to its strong magnitude. This may be related to the spurious oceanic Rossby wave pathway problem, as described by Cai et al. (2005) in a different CSIRO

model that is of slightly higher resolution. Rossby waves from the Pacific into the Indian Ocean generally propagate along the coast of Western Australia as Kelvin waves, but in many climate models, these waves evidently propagate closer to the equator, directly influencing the thermocline off Java (Saji et al. 2006). In our model, this problem does not appear to the extent seen in the model analyzed by Cai et al. (2005) in which, as a consequence, many of the IOD events only peak almost 1 yr following the peak of ENSO. This would result in ENSO–IOD correlation peaking at 1-yr lag, which is also the case in a number of IPCC AR4 models (Cai et al. 2011a), but not in our model (Fig. 3h). Nonetheless, the wind stress pattern over the Pacific associated with the IOBM is qualitatively comparable with that observed. One feature of particular relevance to our discussions is the easterly (westerly) anomalies over the western Pacific corresponding with warm (cool) IOBM and co-occurring El Niño (La Niña).

The biases noted above are not surprising given the coarse model resolution. More importantly though, the CSIRO Mk3L does capture the large-scale climate modes over the Indo-Pacific basins and their interactions. As such, given the model's relatively inexpensive cost for millennial time-scale integrations, CSIRO Mk3L is
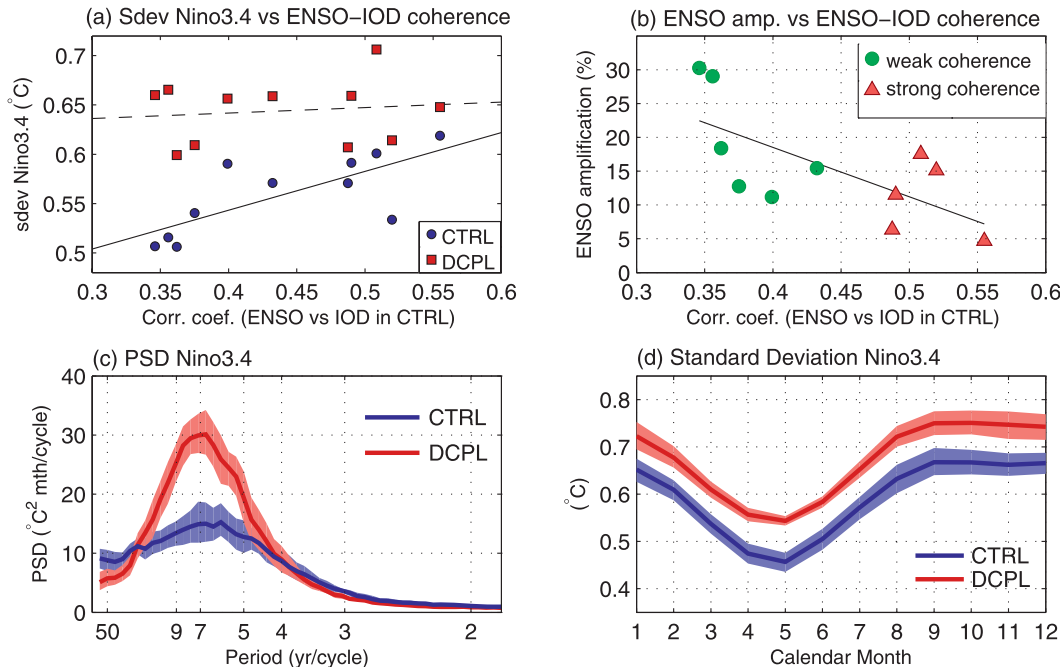
FIG. 5. (a) Standard deviations of Niño-3.4 in CTRL (blue dots) and DCPL (red squares) across the 11 ensemble members as a function of ENSO–IOD coherence in CTRL. (b) Percentage change in Niño-3.4 standard deviation in DCPL relative to CTRL as a function of ENSO–IOD coherence in CTRL across the 11 ensemble members. The ENSO–IOD coherence, which only exists in CTRL, is expressed as a correlation between the first principal components of Indian Ocean SST (August–November) capturing an IOD, and Pacific Ocean SST (September–December) depicting an ENSO. Two different symbols indicate epochs of strong and weak ENSO–IOD coherence. The best-fit lines as estimated via the least squares method are shown in (a) and (b). (c) Power spectra of Niño-3.4 in DCPL (red) and CTRL (blue). Thick curves indicate the ensemble average. (d) Standard deviation of Niño-3.4 at each calendar month in DCPL (red) and CTRL (blue). The color shading in (c) and (d) indicates the estimated 95% confidence intervals using 1000 bootstrapped means each calculated based on 11 random draws with replacement from the corresponding 11 spectrum and standard deviation samples.

particularly useful for studying Indo-Pacific climate feedback interactions across a series of centennial epochs. An important feature to highlight is the longer-lasting ENSO and its consequence on ENSO co-occurrences with the Indian Ocean modes (Figs. 3g,h,i). In that sense, our results may be applicable for understanding the low-frequency component of ENSO in the real system, which is unlikely to be constrained by presently available observations (Wittenberg 2009).

4. Shifts in ENSO dynamics

It is found that ENSO variability is enhanced in all of the 11 DCPL experiments relative to their corresponding 100-yr CTRL epochs (Figs. 5a,b), with an amplification in variance within the period band of 5–10 yr (Fig. 5c). The ENSO period also becomes slightly longer in DCPL, which is qualitatively consistent with some of the previous studies (Wu and Kirtman 2004; Dommenget et al. 2006; Behera et al. 2006). The increases in ENSO variability are not constant across the experiments, which

range from 5% up to 30% (Fig. 5b). An F test suggests that most of these changes are significantly different from 0 at the 95% level (see the appendix). As noted in the appendix, the ENSO variability in DCPL can appear to be slightly weaker when too short a data record is analyzed. These reductions, however, are not significant under an F test. Therefore, our result is in contrast with the previous studies that found weaker ENSO variability (see section 1). Figures 5a,b further illustrate that the degree of the ENSO amplification appears to vary as a function of ENSO–IOD coherence in CTRL. This will be explained further in section 5. Below, we will first explore the dynamical processes responsible for stronger ENSO variability in DCPL.

Changes in ENSO variability are more or less spatially stationary as demonstrated in Fig. 6, which compares the ENSO SST patterns in DCPL and CTRL. The differences are largely associated with amplification of ENSO magnitude over the east-central Pacific (Fig. 6b). There are also no appreciable shifts in the seasonal cycle of ENSO (Fig. 5c). Nevertheless, notable dynamical changes
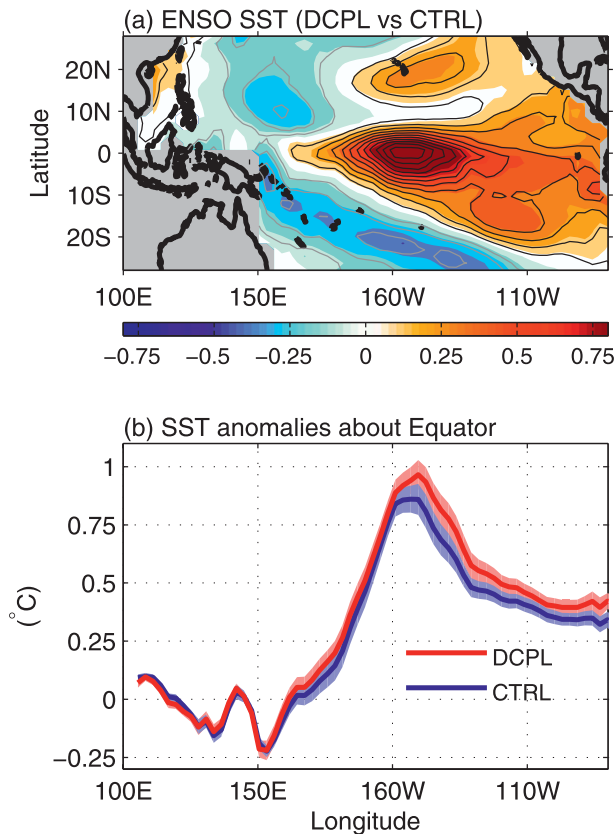
FIG. 6. (a) ENSO-related SST patterns in DCPL (color shades) and CTRL (contours) as extracted from EOF analysis, averaged across the 11 ensemble members. (b) The equatorial profile of the patterns shown in (a) as averaged over 5°S–5°N for DCPL (red) and CTRL (blue). In (b), the solid lines indicate the mean of the 11 ensemble members; the corresponding color shading indicates the 95% confidence interval evaluated using the bootstrap method.

do occur in DCPL with respect to CTRL. As illustrated in Fig. 7, there is overall more notable eastward propagation of SST anomalies along the equatorial Pacific in DCPL, which may indicate a more prominent thermocline mode, as has also been observed post-1980. It is worth noting that the eastward propagation occurring in both DCPL and CTRL is almost exclusively due to the action of the warm SST anomalies (Figs. 7b,c). Such asymmetry is also observed in nature (McPhaden and Zhang 2009), which may be partly set directly or indirectly by the presence of the Indonesian Throughflow (Santoso et al. 2011).

Utilizing the Bjerknes (BJ) index formula as devised by Jin et al. [(2006); see their Eq. (9); see also Santoso et al. (2011); Kim and Jin (2011) for its application], we found that the thermocline feedback is indeed enhanced in DCPL. In essence, the BJ index represents the linear growth rate of ENSO within the context of the recharge oscillator paradigm (Jin 1997), constituting two damping
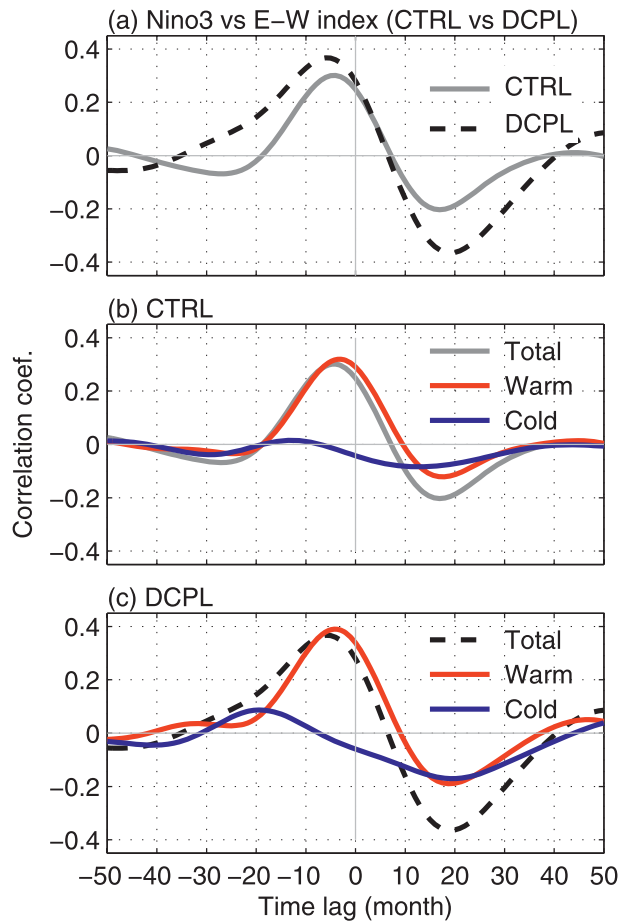

FIG. 7. (a) Lag correlation between the Niño-3 index and an east–west SST index in CTRL (gray) and DCPL (dashed) to diagnose the direction of zonal propagation of SST anomalies, a useful indicator for ENSO dynamics (e.g., Guilyardi 2006). The east–west SST index is defined as the area-averaged SST in the far eastern Pacific (5°S–5°N, 91°–80°W) minus that in the Niño-4 region (5°S–5°N, 160°E–150°W). One could also use the Trans-Niño Index to arrive at the same result. Positive (negative) time lags indicate the E–W index leading (lagging) Niño-3. As such, positive (negative) correlations at negative (positive) time lags indicate eastward-propagating SST anomalies (Santoso et al. 2011, their Figs. 7 and 13). Also shown is the decomposition of the total lag correlations in (b) CTRL and (c) DCPL into contributions by positive and negative Niño-3 anomalies. These warm and cold contributions are separated by computing the respective covariances according to positive/negative Niño-3 anomalies keeping the total standard deviation (i.e., accounting all anomalies) in the denominator. Correlation magnitude greater than ≈0.1 is significant above the 95% level. The difference between the correlation maxima at negative and positive time lags is taken to indicate the prominence of eastward propagation. These diagnostic values are calculated from the total correlations in (a) yielding an average of 0.53 and 0.75 for CTRL and DCPL, respectively, with a 95% confidence interval of about ±0.1. This indicates that this measure is significantly larger for DCPL than CTRL, suggesting more prominent eastward propagation in DCPL.
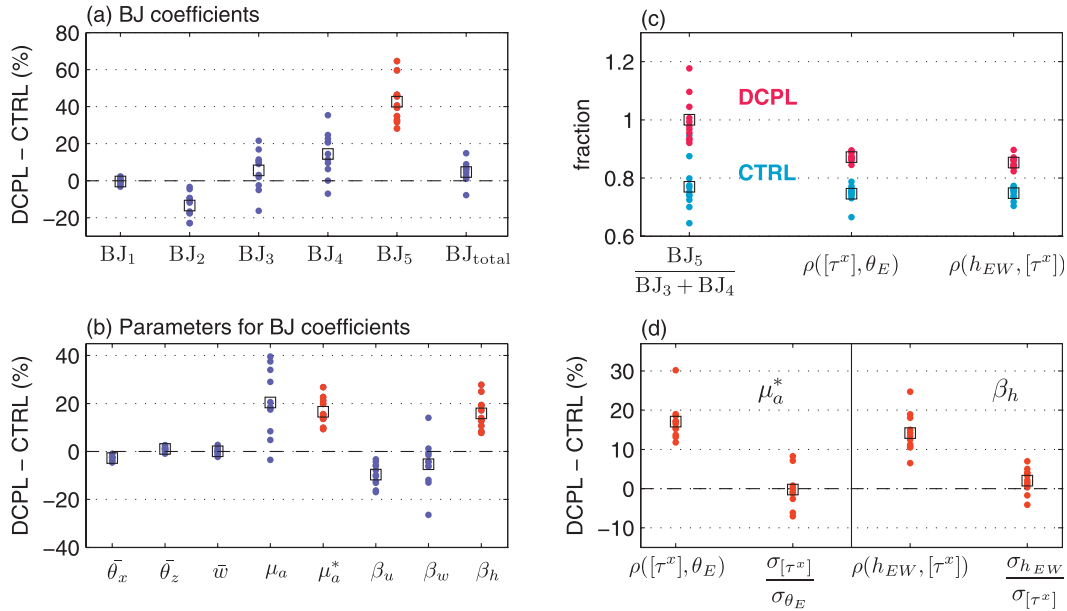
FIG. 8. The differences between DCPL and CTRL expressed as a percentage change for (a) BJ index coefficients and (b) various coupling parameters and climatological variables that constitute the BJ index coefficients (see text for description). In (a), red dots highlight the component with the largest difference (i.e., the thermocline feedback term BJ_5). In (b), red dots correspond to the coupling parameters that constitute BJ_5. All original values in (b) are positive, so a positive (negative) change indicates stronger (weaker) values in DCPL. (c) Various diagnostic terms: ratio of BJ_5 to $[BJ_3 + BJ_4]$ as a measure of the importance of thermocline feedback relative to local feedbacks (zonal advective and Ekman pumping), correlation $\rho(y, x)$ between zonally integrated equatorial Pacific zonal wind stress $[\tau_x]$ and eastern Pacific SST θ_E, and correlation between east–west equatorial Pacific thermocline slope h_{EW} and $[\tau_x]$ (red and blue dots indicate values in DCPL and CTRL, respectively). (d) Percentage change of correlation and standard deviation ratio that constitutes the regression coefficients μ_a^* and β_h in DCPL relative to CTRL: $\mu_a^* = \rho([\tau^x], \theta_E) \times (\sigma_{[\tau^x]}/\sigma_{\theta_E})$; $\beta_h = \rho(h_{EW}, [\tau^x]) \times (\sigma_{h_{EW}}/\sigma_{[\tau^x]})$. The squares in (a)–(d) indicate mean values.

terms by the mean currents (BJ_1) and the net air–sea heat fluxes (BJ_2), and three destabilizing terms: zonal advective (BJ_3), Ekman pumping (BJ_4), and thermocline (BJ_5) positive feedback terms, each of which is a function of air–sea coupling strengths and the mean climate. For instance, BJ_5 is a product of three terms: 1) β_h, sensitivity of the east–west thermocline slope in response to the zonally integrated zonal wind stress τ^x over the equatorial Pacific; 2) μ_a^*, sensitivity of the basin-wide τ^x to the local SST anomalies in the eastern Pacific; and 3) $\overline{w}$, the local mean upwelling velocity [see Santoso et al. (2011) for description of the other BJ terms]. We compute the coupling parameters via linear regression using 100-yr monthly data in each of the 11 runs of both DCPL and CTRL.[1]

The change in the BJ indices and the governing parameters in DCPL relative to CTRL are shown in Fig. 8. The strength of the BJ terms generally increases, except that of the mean currents (BJ_1), which exhibits negligible change (Fig. 8a). This is expected since the mean climate exhibits only little change in response to a decoupled Indian Ocean (e.g., Fig. 8b). It should be noted that although the change in the mean climate is small, there is a slight cooling over the central Pacific across the 11 ensembles (see discussion in section 6 and Fig. 15). This central Pacific cooling contributes to the slight weakening of the zonal SST gradient $\overline{\theta_x}$ (Fig. 8b) and, thus, aids in limiting increases in the strength of the zonal advective feedback (BJ_3). Overall though, the ENSO response is largely dominated by an enhanced thermocline feedback (BJ_5). Note that the enhanced thermocline feedback is also accompanied by its increased importance relative to the local feedbacks (see Fig. 8c), consistent with the emergence of more apparent eastward-propagating SST anomalies in DCPL (Fig. 7).

The enhanced thermocline feedback in DCPL stems from its stronger β_h and μ_a^* air–sea coupling parameters

---

[1] To focus on processes over ENSO time scales, linear trends and variabilities with periods shorter than 2 yr have been removed prior to the analysis. The governing SST equation is based on the upper 50 m in the eastern Pacific within the core region of ENSO SST, capturing the Niño-3.4 and Niño-3 regions (5°S–5°N, 170°–90°W). The upper 300-m heat content is used as a proxy for thermocline depth.

(Fig. 8b). Since these parameters are expressed as regression coefficients, they are by definition the product of correlation between the governing variables and the ratio of their standard deviations (see Fig. 8d). It turns out that this enhanced coupling is largely associated with the stronger underlying positive correlations (Figs. 8c, d), that is, the correlations between both local SST and the east–west thermocline tilt, and the zonally integrated τ^x across the equatorial Pacific. These enhanced correlations are essentially due to weakened τ^x variability over the western Pacific, which occurs predominantly in the first half of the calendar year (Fig. 9a). Forming part of the anomalously strong (weak) Walker circulation associated with La Niña (El Niño), the western Pacific τ^x is negatively correlated with eastern Pacific SST, having a counteracting influence on the ENSO-enhancing wind anomalies farther east (see, e.g., Fig. 2). Thus, it is expected, as demonstrated in Fig. 9b, that its weaker variability promotes an increase in the basin-wide positive correlation, which is determined largely by the wind anomalies over the east-central Pacific. This reflects an increased air–sea coupling that underlies a stronger ENSO thermocline feedback as described above. As will be apparent in section 5, the weaker western Pacific τ^x anomalies in DCPL are consistent with the absence of the IOBM in those runs.

5. Role of the Indian Ocean

As shown in section 4, the enhanced ENSO variability in DCPL is accompanied by weaker τ^x anomalies over the western Pacific, which occur predominantly during January–May (Fig. 9a). Figure 10 presents the composite evolution of τ^x anomalies across the Indian and Pacific Oceans associated with El Niño and La Niña in CTRL and DCPL. The contours overlaid on Figs. 10a,d indicate the patterns of the observed ENSO τ^x anomalies for comparison. The τ^x anomalies over the western Pacific in CTRL, DCPL, and the observations switch to easterlies (westerlies) at the peak of El Niño (La Niña) around Sep(0)–Dec(0), persisting through the following months. The differences in the anomaly magnitude over the western Pacific ($\approx$120°–150°E) between DCPL and CTRL are largest and statistically the most significant over this follow-up period (Figs. 10c,f). Specifically, the easterly (westerly) anomalies are weaker in DCPL following the peak of El Niño (La Niña). This illustrates that the reductions of the western Pacific τ^x variability in DCPL, which occur over the first half of the calendar year, appear to be associated with the decay phases of ENSO. This is because in CTRL (and observations) it is the decay phases of El Niño (La Niña) that most often coincide with the easterly (westerly) τ^x anomalies over
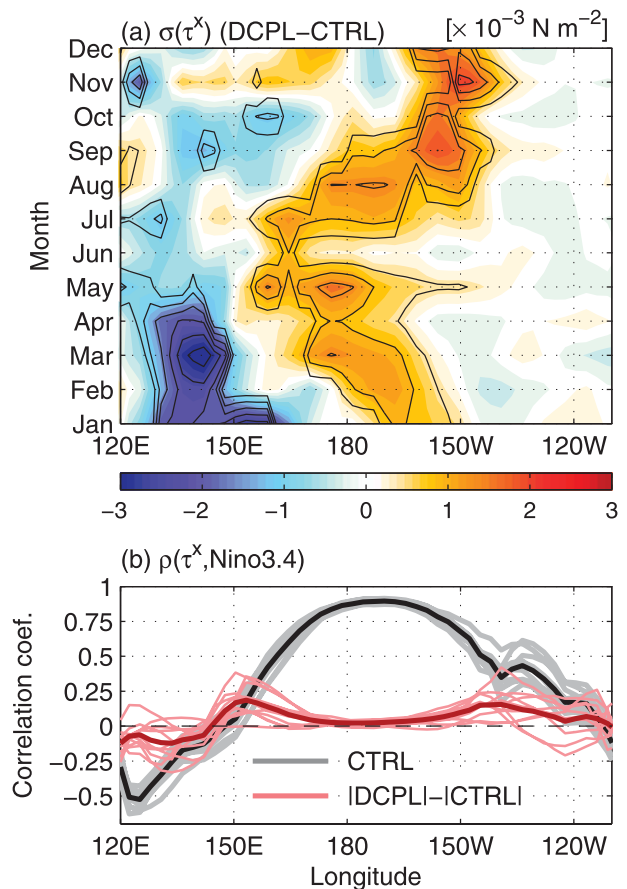

FIG. 9. (a) Difference in the standard deviations of the equatorial zonal wind stress (5°S–5°N) in DCPL and CTRL. The black contours indicate the differences that are significantly different from zero at the 95% level as inferred from a bootstrap method with 1000 simulations using the 11 samples. (b) Correlation between the equatorial zonal wind stress and the Niño-3.4 index in CTRL (gray) and the difference in the correlation magnitude between DCPL and CTRL (pink). The darker curves denote the corresponding mean value.

the western Pacific, which are enhanced by warm (cool) IOBM (see section 3 and further below). These Indian Ocean basin-wide anomalies are obviously absent in the DCPL simulations.

The effect that the missing IOBM would have on western Pacific τ^x in DCPL as inferred from Figs. 10c,f is expected to be underestimated. This is because as the ENSO SST anomalies become enhanced in DCPL, the western Pacific τ^x anomalies would also become stronger, as they are linked. Furthermore, note that in the model the western Pacific easterlies (westerlies) also occur during ENSO's developing phase, which includes boreal winter through autumn of the same year as the peak of ENSO [Jan(0)–May(0)], in contrast with observations (Figs. 10a,d). This is due to the model's ENSO events that are long lasting (Figs. 3a,g). Also associated
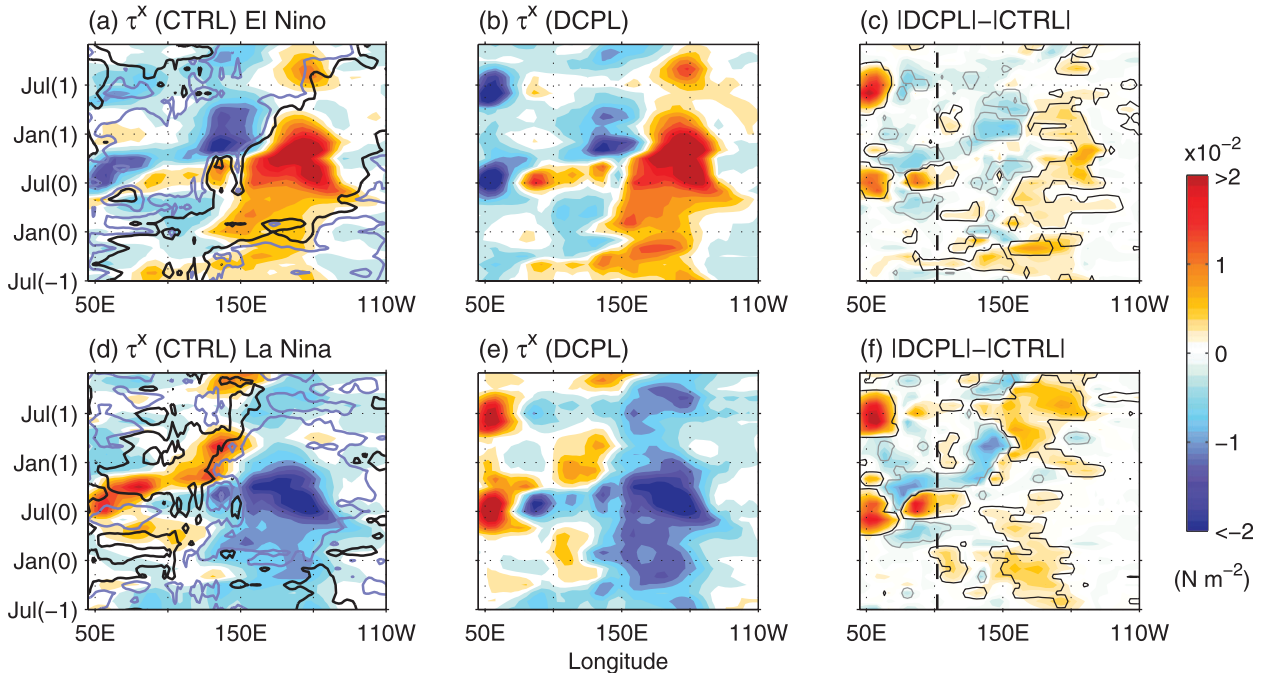
FIG. 10. Evolution of zonal wind anomalies over the Indian and Pacific Oceans composited based on (a)–(c) El Niño and (d)–(f) La Niña for (a),(d) CTRL and (b),(e) DCPL. The corresponding differences in the anomaly magnitude between DCPL and CTRL are shown in (c) and (f). In (a),(d), black and blue contours mark the position of the NCEP–NCAR reanalysis ENSO wind anomalies (1970–2006). In (c),(f), anomalies that are significant above the 90% level are contoured. The vertical dashed line marks the boundary separating the Pacific from the Indian Ocean.

with the long-period ENSO is the occurrence of IOBM during ENSO's developing phase in CTRL, which is indicated by the positive correlation at 0 lag in Fig. 3i. Despite the stronger ENSO in DCPL, the strength of the western Pacific τ^x anomalies between DCPL and CTRL is not statistically different during Jan(0)–May (0), thus somewhat revealing the effect of a missing IOBM in DCPL during this phase (Figs. 10c,f). This effect is certainly not as prominent as that during the ENSO mature/decay phase over which IOBM occurrences are much more frequent in CTRL (Fig. 3i).

The role of the western Pacific easterly (westerly) τ^x anomalies on ENSO phase transition is key to the western Pacific oscillator paradigm for ENSO as described by Weisberg and Wang (1997). In that paradigm, the western Pacific easterly (westerly) τ^x force eastward-propagating upwelling (downwelling) Kelvin waves that dampen the ENSO thermocline anomalies in the east (Wang et al. 1999). Within the recharge oscillator framework, the effect of easterly (westerly) wind anomalies over the western Pacific during El Niño (La Niña) is to weaken the dominance of the central Pacific westerly (easterly) τ^x anomalies on the zonally integrated wind stress, which balances the anomalous eastward (westward) thermocline tilt. Slackening of this basin-wide

wind stress leads to thermocline adjustment toward a discharge (recharge) of the equatorial Pacific upper-ocean heat content. These western Pacific wind anomalies occur following the peak of ENSO, and in the observations and CTRL they are enhanced by the IOBM, leading to the decay of ENSO events (Kug and Kang 2006). In CTRL, however, this process can occur during the ENSO developing phase given the model's long-lasting ENSO. The absence of IOBM during ENSO's growth and mature phase in DCPL is consistent with increased air–sea coupling, which sustains the thermocline feedback (i.e., stronger μ_a^* and β_h; Figs. 8b,d; see section 4), thus favoring ENSO growth and slower transition into ENSO's opposing phase. The missing IOBM is thus consistent with the stronger ENSO and its longer period in DCPL.

The stronger ENSO across all DCPL simulations suggests that the Indian Ocean in CTRL exerts a net damping on ENSO variability. This could imply the dominance of the IOBM damping effect in the model. However, the increase in ENSO variability in DCPL relative to CTRL is found to be highly correlated to the coherence between ENSO and IOD in CTRL across the eleven 100-yr epochs (Fig. 5b), not to the ENSO–IOBM coherence, which is not statistically significant. The

correlation with ENSO–IOD coherence is negative (≈ -0.7) and significant at the 98% confidence level. This significant correlation arises largely due to the fact that epochs with stronger ENSO–IOD coherence in CTRL tend to have larger ENSO variability (see Fig. 5a), as expected given ENSO conditions can trigger IOD development. Within the context of Indian Ocean feedback, however, the negative correlation in Fig. 5b may suggest that the net negative feedback exerted by the Indian Ocean on ENSO is weaker (stronger) during epochs when the ENSO–IOD coherence is stronger (weaker). Below we reveal the reason that gives rise to this relationship. For brevity, in the rest of the discussion the strong and weak ENSO–IOD coherence epochs are hereafter referred to as *strong* and *weak coherence*, respectively.

Figures 11a–d present the composite evolution of ENSO-related SST anomalies in CTRL over the Indo-Pacific region, across all epochs segregated according to years when El Niño (La Niña) and positive (negative) IOD coincide, and years when they do not. The number of instances used to form the composites is shown in each figure panel. The IOBM patterns are apparent during the ENSO mature/decay phase in both IOD and non-IOD cases (Figs. 11a–d). As IOBM is largely a response to ENSO, their intensity depends on ENSO magnitude; that is, the stronger the ENSO, the stronger the IOBM that follows. However, IOBM patterns do also occur during ENSO's developing phase in CTRL but emerge only in the non-IOD case (Figs. 11b,d). As such, by definition of ENSO–IOD coherence, the less frequently ENSO and IOD co-occur within an epoch (i.e., weak coherence), the more frequently the developing ENSO events would coincide with IOBM patterns. For succinctness, the rest of the discussion mainly refers to El Niño, positive IOD, and warm IOBM. As demonstrated in Figs. 11e–h, by further segregating the composites in Figs. 11c,d into weak and strong coherence epochs, the peculiar IOBM patterns indeed appear more intense for the non-IOD composites of the weak coherence epochs than strong coherence epochs (Figs. 11f,h). In short, this analysis suggests that in CTRL the developing ENSO tends to coincide with either the IOD or IOBM events. Thus, the developing ENSO tends to co-occur with IOBM more frequently during weak ENSO–IOD coherence epochs. These peculiar IOBM occurrences are expected given the long-period ENSO in the model (see Fig. 3).

The more prevalent IOBM anomalies, and the less frequent co-occurring IOD, during ENSO's growth phase have an important implication for ENSO genesis. To illustrate this, we conduct a set of 11 atmosphere-only model experiments by forcing the AGCM with anomalous SST patterns in the Indian Ocean as represented by the first EOF mode of SST at each calendar month in each of the eleven 100-yr epochs in CTRL. From December to May, a typical IOBM pattern is used to force the model, and an IOD-type pattern is employed for the remaining months. In another set of experiments, ENSO SST anomalies are inserted in the Pacific sector only. In a third set, the AGCM is forced by both Indian Ocean and ENSO anomaly patterns. The typical anomalous SST patterns and forcing domains can be gleaned from Fig. 2, and their seasonal patterns of evolution are shown later (Fig. 13c). These anomalies are added onto the seasonally varying observed climatological SST fields that are also prescribed outside the domains. It is important to note that the monthly EOF SST pattern for ENSO in January–May corresponds to the decay phase of ENSO when the eastern Pacific anomalies are stronger than those in the previous year, coinciding frequently with IOBM occurrences [see, e.g., Jan(1)–May(1) in Fig. 11]. Moreover, the Indian Ocean SST forcings are chosen to be well confined within the interior of the Indian Ocean (i.e., excluding the Indonesian seas, which are otherwise included as part of the Pacific domain; see Fig. 2). This point helps to illustrate the extent to which SST anomalies generated within the enclosure of the Indian Ocean can directly influence the Pacific climate.

Figure 12a presents the equatorial τ^x anomalies in response to El Niño SST, showing warm SST-induced westerly anomalies over the central Pacific. Easterly anomalies are seen in the western Pacific during boreal winter–spring due to SST warming over the South China Sea and the cold ENSO horseshoe pattern (see Fig. 2a,b; also Lau and Nath 2003, their Fig. 4; and Wang et al. 2006). As expected, the El Niño rainfall response shows anomalously high and low precipitation amounts over the eastern and western Pacific, respectively (Fig. 12b). In Fig. 12c, the easterly anomalies due to warm IOBM during the boreal winter–spring extend into the western Pacific, whereas those due to the IOD in June–November are mainly confined to within the Indian Ocean. The impact of the IOBM-induced winds is apparent in Fig. 12e with the forcing of both Indian Ocean and ENSO SSTs; that is, this effect strengthens the easterly anomalies in the western Pacific but weakens the central Pacific westerly anomalies (see also Fig. 12g). Such anomalous atmospheric responses due to the Indian Ocean SST modes are consistent with those found by Annamalai et al. (2005), who showed using atmospheric models that positive IOD forcing induced little influence over the Pacific basin (Ohba and Ueda 2007). Annamalai et al. (2005) argue that this is due to the destructive interference of Kelvin waves in response to zonal diabatic heating
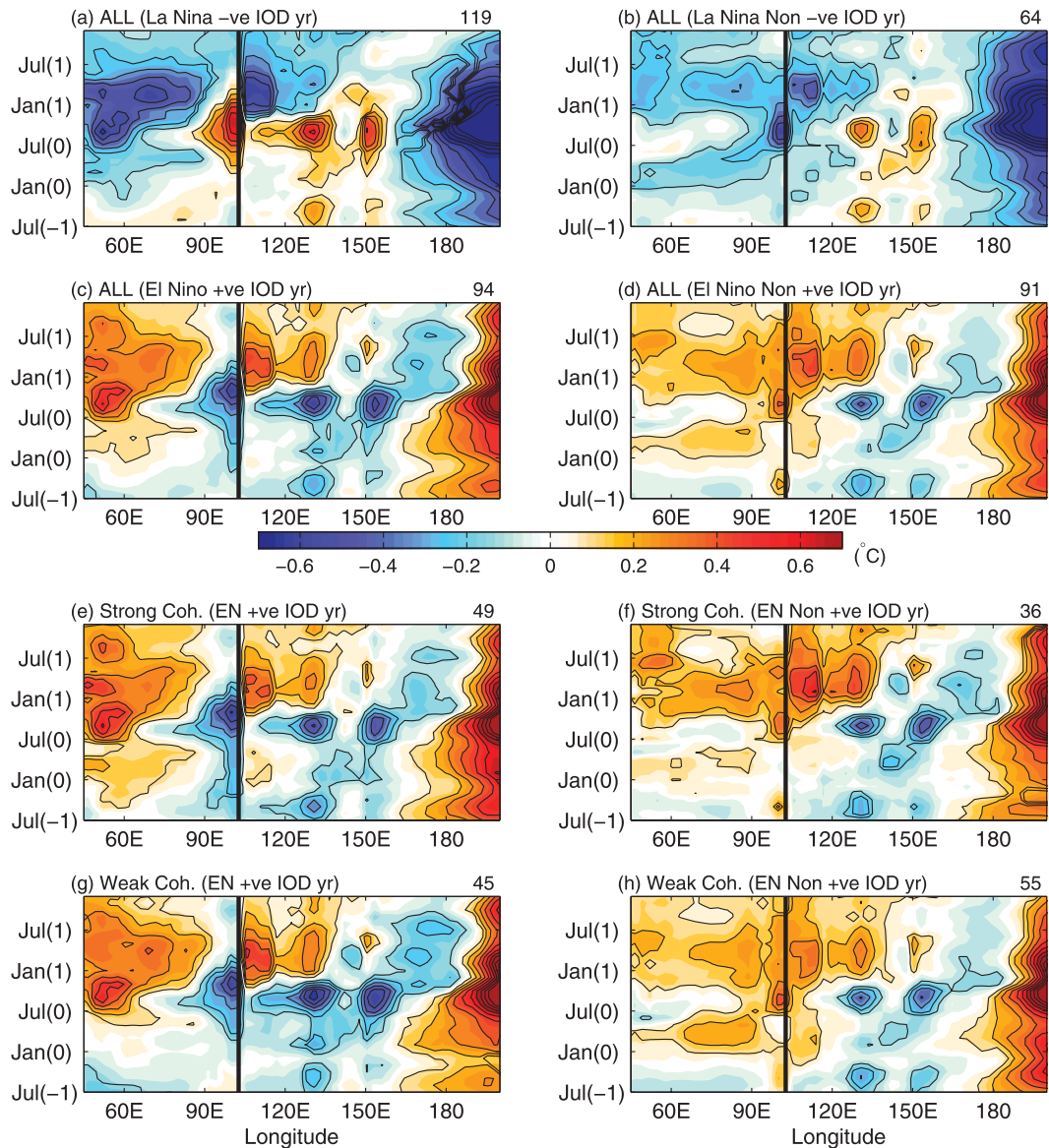
FIG. 11. Composites of SST anomalies along the equator over the Indo-Pacific region based on ENSO years that coincide with IOD events over all epochs for (a),(b) La Niña and negative IOD and (c),(d) El Niño and positive IOD. (e)–(h) As in (c),(d), but for the epochs of (e),(f) strong and (g),(h) weak ENSO–IOD coherence. El Niño years are defined when the Niño-3.4 averaged over September–December is above one standard deviation. The IOD and non-IOD years are defined when the principal component of the EOF analysis for tropical Indian Ocean SST averaged over August–November is above and below half of the standard deviation. The contours highlight composites that are significant at the 95% significance level. The solid vertical line marks the boundary separating the western Pacific from the Indian Ocean.

anomalies of opposite sign across the equatorial Indian Ocean. This mechanism appears to operate in our experiments as supported by the positive and negative precipitation anomalies across the equatorial Indian Ocean (Fig. 12d). On the other hand, as is also consistent with Annamalai et al. (2005), warm basin-wide anomalies, which tend to induce only positive precipitation anomalies

over the Indian Ocean (Fig. 12d), force easterly wind anomalies over the western Pacific as part of the atmospheric Kelvin wave response to this uniform diabatic heating (Fig. 12c). Repeating these experiments with the model SST climatology as boundary condition for the AGCM does not alter the result; that is, the IOBM exerts stronger influence on the Pacific than the IOD (Figs. 13a,b).
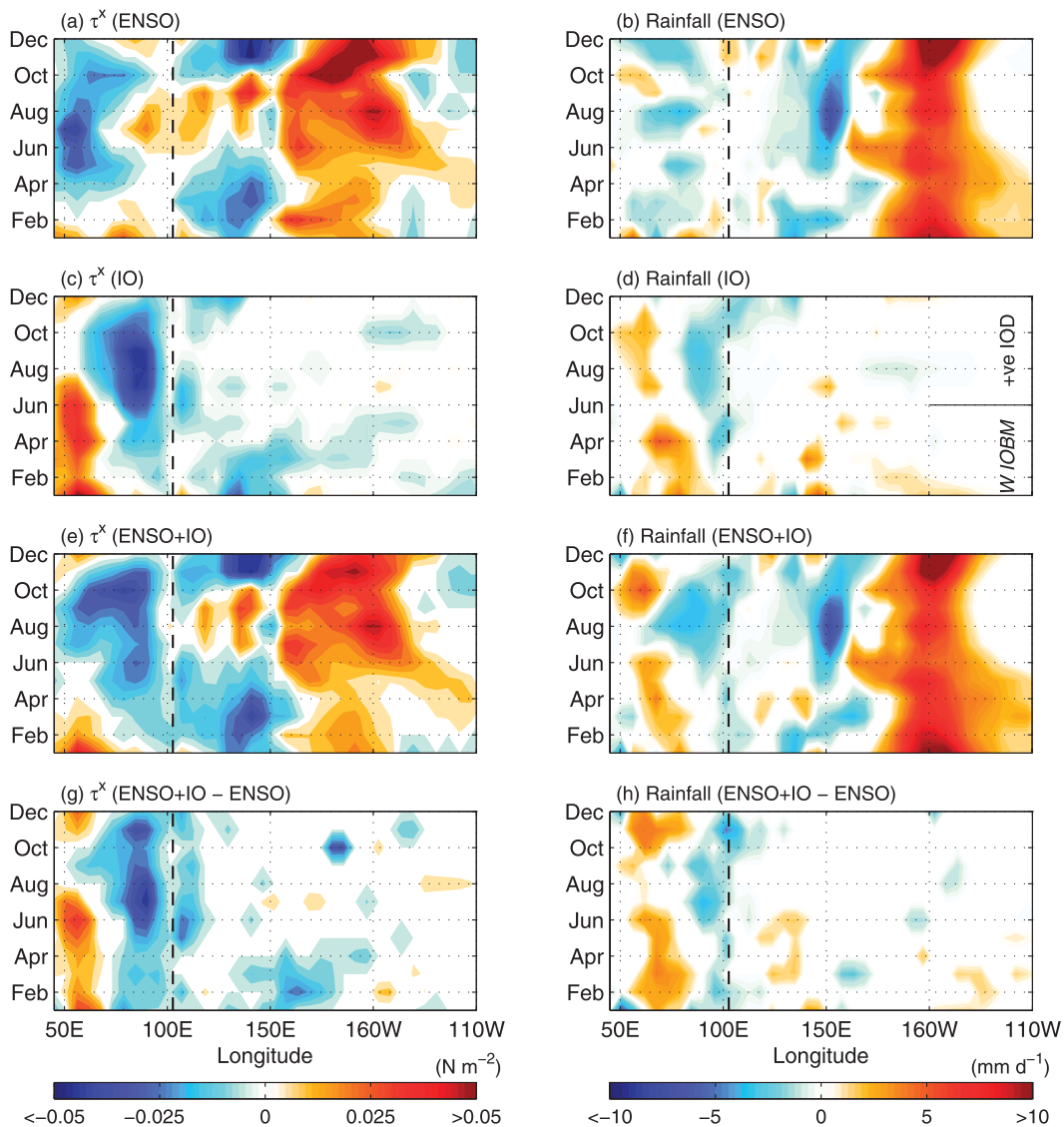
FIG. 12. (left) Zonal wind anomalies and (right) precipitation anomalies along the equator (5°S–5°N) averaged over the 11 ensembles of AGCM experiments (see text) in response to (a),(b) El Niño SST patterns, (c),(d) Indian Ocean SST patterns (IOBM anomalies for December–May; IOD anomalies for June–November), and (e),(f) ENSO and Indian Ocean SST patterns combined. (g),(h) The difference between (e),(f) and (a),(b), respectively. Only fields that are significantly different from zero at the 95% level are shown. The SST patterns are represented as the first EOF mode of SST at each calendar month over the respective domains shown in Fig. 2 (see text in section 5 for further details).

Our AGCM results above appear at first sight to be partially at odds with the findings of previous studies (Izumo et al. 2010; Luo et al. 2010; Fischer et al. 2005), which suggested that the IOD can enhance ENSO-related wind anomalies, as has apparently been seen in observations (e.g., Saji and Yamagata 2003). Because the IOD in our decoupled Pacific CGCM experiments, whose magnitude is largely retained, does not force notable changes over the Pacific (not shown), this discrepancy

does not seem to be related to the shortcomings in the use of SST-forced AGCM runs in general, as noted for example by Kirtman and Vecchi (2011). The cold and dry bias over the warm pool region in our model can underestimate the effect of the IOD, particularly in the eastern Indian Ocean (Fig. 4), and this is only partly offset by the strong IOD amplitude (figure not shown). However, the AGCM experiments discussed above are forced with observed SST climatology (Fig. 12), so this
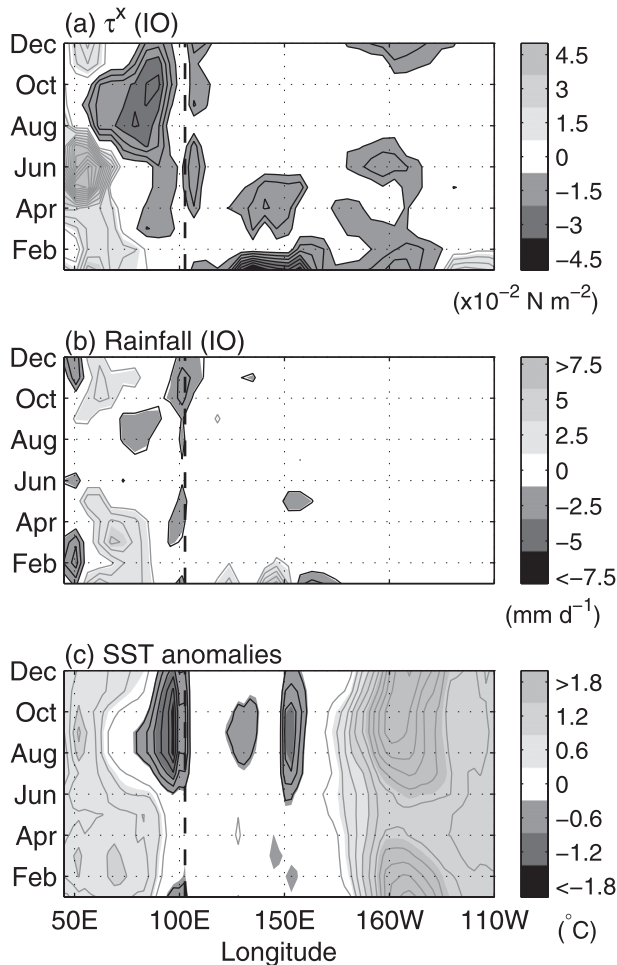
FIG. 13. (a) Zonal winds and (b) rainfall response to Indian Ocean SST anomalies, as in Figs. 12c,d, but with SST climatology diagnosed from the 1100-yr coupled model integration. (c) The monthly evolution of SST anomalies used to force the AGCM experiments, shown here averaged between 5°S and 5°N across the 11 ensemble members. Positive (negative) values are indicated by lighter (darker) shading.
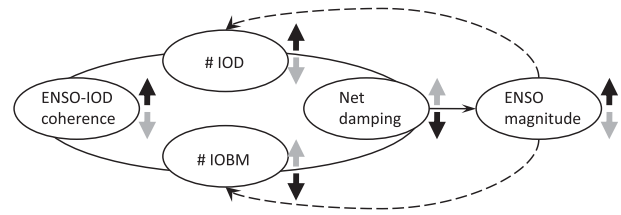

FIG. 14. Schematic illustrating the Indo-Pacific feedback interactions in CTRL epochs influencing the strength of ENSO variability as described in section 5. Black (gray) thick arrows correspond with strengthening (weakening) ENSO magnitude. Upward (downward) thick arrows indicate an increase (decrease) in the respective variables. Solid (dashed) thin arrow indicates Indian Ocean (ENSO) influence on ENSO (the Indian Ocean). The role of the Indian Ocean on ENSO variability is a net damping as revealed by the DCPL experiments. This net negative feedback is dominated by the IOBM via enhancement of the western Pacific zonal wind anomalies that weaken the ENSO Bjerknes feedback wind component farther east. Relative to the IOBM, the IOD is more conducive for ENSO growth (Fig. 12). The IOBM is a prominent feature that co-occurs with developing ENSO during non-IOD years (Fig. 11). As such, the extent of this damping appears to be determined by the strength of ENSO–IOD coherence, which reflects the relative frequency of IOD and IOBM co-occurrences with ENSO. The stronger the ENSO–IOD coherence, the less frequently ENSO growth coincides with the IOBM, the weaker the net damping, and the stronger the ENSO variability.

The analysis above reveals the relative role of the IOD and IOBM on ENSO. The extent of their net effect depends on the relative frequency of their co-occurrences with ENSO, which is indicated by the strength of the ENSO–IOD coherence. As revealed by the DCPL experiments, the Indian Ocean exerts a net negative feedback on ENSO variability in each of the CTRL epochs. Therefore, the IOBM damping, via enhancement of the western Pacific τ^x anomalies, appears to dominate the feedback effect on ENSO in CTRL. In essence, these results suggest that the stronger the ENSO–IOD coherence, the less (more) frequently the IOBM (IOD) coincides with developing ENSO events and, thus, the weaker the net negative feedback on ENSO variability. These feedback interactions are summarized in Fig. 14 and are also depicted by the negative correlation shown in Fig. 5b.

6. Discussions and conclusions

This study aims to demonstrate a link between Indo-Pacific feedback interactions and ENSO dynamics via an ensemble set of Indian Ocean decoupling experiments with a CGCM, each one century long, within a 1100-yr preindustrial climate simulation. It is found that an absence of this interbasin feedback in the model allows the ENSO variability to amplify and its period to

partially removes the model bias. It is possible then that SST anomalies over Indonesian seas, which are possibly related to the IOD, can have a strong impact on Pacific atmospheric circulation (Annamalai et al. 2010). By including this region as part of the Indian Ocean, for example in the experiment of Yu et al. (2002), the IOD influence on ENSO may be enhanced. In our experiments, the IOD eastern pole excludes any portion of the western Pacific. Nonetheless, in agreement with Annamalai et al. (2005), our experiments suggest that relative to the IOBM, the IOD is seen to be more favorable for ENSO growth. Thus, in that sense this is still consistent with the previous studies (e.g., Izumo et al. 2010; Luo et al. 2010).

increase. These findings are in agreement with the results of Dommenget et al. (2006); Jansen et al. (2009), who used a simple recharge oscillator model fitted to observations; and Frauen and Dommenget (2012) with their hybrid coupled model. Utilizing the BJ index formula as devised by Jin et al. (2006), we further show that the underlying thermocline mode is enhanced. This is evidenced by the more prevalent eastward-propagating equatorial Pacific SST anomalies in DCPL. The more prominent ENSO thermocline mode arises from stronger coupling between the eastern Pacific SST, and east–west thermocline slope, to the basin-wide equatorial Pacific zonal winds. This stronger coupling is reflected from the stronger correlations between the zonally integrated wind stress and the oceanic variables, owing to the weaker western Pacific wind anomalies (easterlies in El Niño case) that generally act as a negative feedback on ENSO. This is shown to be consistent with the absence of IOBM anomalies in DCPL that otherwise tend to enhance these ENSO-damping wind anomalies.

The possible link between Indo-Pacific feedback interactions and ENSO dynamics is an important yet complex research topic. This present study is motivated by the possible shift in ENSO dynamics toward a more prominent thermocline mode since the late 1970s, as accompanied by increasing ENSO–IOD co-occurrences (Fig. 1). Demonstrating such an epochal link is difficult, due to the relatively sparse observational data and the strong dependence of the Indian Ocean anomalies on ENSO. The latter makes it difficult to tease out the feedback processes involved, unless the Indian Ocean can be artificially decoupled from the ENSO system.

Although our ensemble experiments exhibit a range of ENSO responses to a noninteractive Indian Ocean, the ENSO variability across experiments is consistently enhanced. This reveals that the net effect of the Indian Ocean in CTRL is a damping on ENSO. The degree of ENSO damping in the CTRL epochs is found to be negatively correlated to the strength of the ENSO–IOD coherence. Composite analysis reveals that, during non-IOD years in CTRL, IOBM anomalies often coincide with growth phases of ENSO. This is associated with the long-period ENSO that the model simulates. As such, in 100-yr epochs over which ENSO and IOD coincide more frequently, there are fewer IOBM occurrences during the ENSO developing phases. AGCM experiments forced by Indo-Pacific SST forcings show that the IOBM enhances easterly (westerly) wind anomalies in the western Pacific associated with a maturing El Niño (La Niña). These tend to weaken the equatorial central Pacific anomalous winds that constitute the Bjerknes positive feedback for ENSO growth. Within the recharge-oscillator framework for ENSO dynamics,
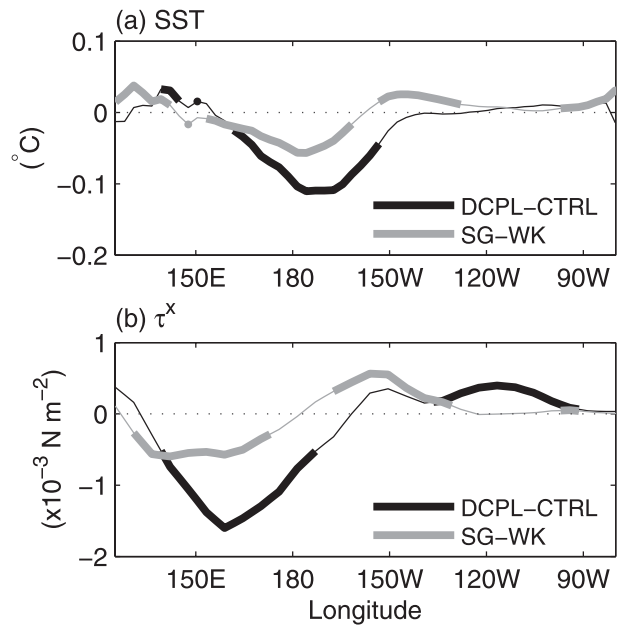

FIG. 15. Differences in (a) mean SST and (b) zonal wind stress over the equatorial Pacific between DCPL and CTRL (black) and strong and weak ENSO–IOD coherence epochs (gray). Statistically significant changes at the 95% level are indicated with thick lines.

this would weaken air–sea coupling that governs the ENSO thermocline mode. Furthermore, the AGCM experiments show that the IOD on the other hand does not generate any wind anomalies that may interrupt ENSO growth processes, at least in this model and if the Indonesian seas are excluded (see section 5). As such, relative to the IOBM, IOD conditions are still favorable for ENSO growth, and so the IOD still has a net enhancing effect (i.e., consistent with, e.g., Izumo et al. 2010; Luo et al. 2010). Therefore, our analysis suggests that net negative feedback exerted by the Indian Ocean on ENSO is weaker within epochs in which developing ENSO events are more frequently accompanied by the IOD, and less frequently by the IOBM (see schematic Fig. 14).

The fact that ENSO–IOD coherence varies across epochs suggests a link with the background climate. Figure 15 shows the difference in SST and zonal wind stress between the strong and weak ENSO–IOD coherence epochs, and between DCPL and CTRL. The statistically significant features, although weak in magnitude, include the cooler central Pacific and the stronger easterly trade winds to the west, both in DCPL and strong ENSO–IOD coherence epochs. This suggests that the climate state in strong coherence epochs is closer to that in DCPL. The degree of Indian Ocean damping in strong-coherence epochs is also closer to
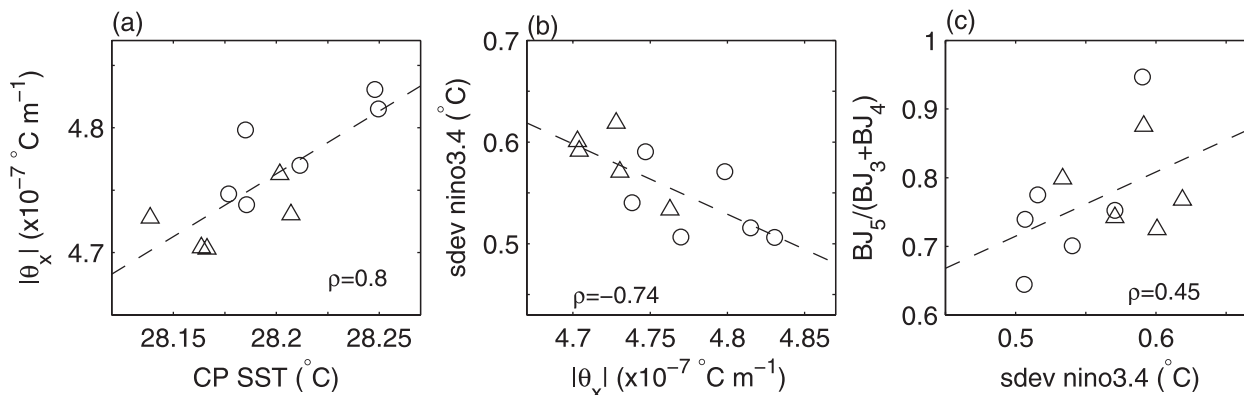
FIG. 16. Relationships between various variables across the 11 epochs in CTRL: (a) strength of zonal SST gradient over east-central Pacific $|\theta_x|$ vs central Pacific SST (5°S–5°N, 160°E–156°W), (b) standard deviation of Niño-3.4 vs $|\theta_x|$, and (c) ratio of BJ_5 to $(BJ_3 + BJ_4)$ vs standard deviation of Niño-3.4. Triangle and circle markers correspond to strong and weak coherence epochs, respectively.

that in DCPL in which there is no damping. These similar tendencies may suggest a link between Indo-Pacific feedback and the mean climate. The climate shift in DCPL is certainly stronger, because of the larger perturbation applied to the system in DCPL. The causes of these somewhat subtle climate shifts are not immediately apparent and will be explored in the future. It is possible though that these outcomes may result from nonlinear feedback responses within the Indo-Pacific climate system that may arise from the asymmetry nature of ENSO (e.g., Okumura and Deser 2010).

The central Pacific mean cooling can be either seen as a westward intrusion of the Pacific cold tongue, or as a contraction of the warm pool. Within the context of ENSO dynamics, either way this leads to a decrease in the equatorial zonal SST gradients, which in turn weakens the ENSO zonal advective feedback. As such, the importance of the thermocline mode relative to the local mode can be enhanced. This mechanism is illustrated in Fig. 16 using correlations across the CTRL epochs: cooler SST Pacific leads to a weaker zonal SST gradient (Fig. 16a), which in turn results in stronger ENSO amplitudes (Fig. 16b) via the increased importance of the thermocline mode (Fig. 16c; Santoso et al. 2011). The weak and strong ENSO–IOD coherence epochs are indicated in Fig. 16, showing that strong coherence epochs generally correspond with stronger ENSO and thermocline feedback. Note that the correlations between ENSO amplitude and the BJ indices (e.g., Fig. 16c) are not highly significant across the epochs, which is expected. This is because the BJ index formula does not take nonlinearity, seasonality, and stochastic noise into account, as has also been noted by Kim and Jin (2011). The BJ index formula is based on assumptions framed within the recharge oscillator paradigm, which itself is not a perfect paradigm for ENSO. However, the BJ index

formula is particularly useful for diagnosing dynamical changes arising from pronounced perturbations, as has been shown here using DCPL, and in recent studies [Santoso et al. (2011) on closure of the Indonesian Throughflow; Kim and Jin (2011) on global warming].

The fact that the DCPL result is found to vary across different epochs suggests a possibility that conflicting results among previous studies may be due to differences in the mean climate across the models that are most apparently due to intrinsic model biases. In particular, as shown by Saji et al. (2006) in IPCC AR4 models, biases in the mean climate are likely to cause different patterns of behavior in Indian Ocean anomalies and the extent to which these respond to ENSO. Simulation of Indian Ocean variability can also in turn determine the realism of an ENSO simulation, as demonstrated by Yu et al. (2009) concerning the overly dominant biennial ENSO in their model arising from Indian Ocean warm bias. Decoupling the Indian Ocean in their model removes this biennial bias and, thus, gives the impression that the ENSO magnitude weakens and its period lengthens. In our model, the occurrences of the IOBM during ENSO growth phases are a consequence of the long ENSO period, which seems to be more related to the issue surrounding model resolution. Nonetheless, in competition with IOD occurrences, this gives rise to varying degrees of Indian Ocean damping across epochs. Thus, decoupling the Indian Ocean results in various ENSO amplifications in DCPL that appear to be negatively correlated with the ENSO–IOD coherence in CTRL (Fig. 5b). Given biases exist to various extents in climate models, it is likely that the degree of damping and the enhancing effects of the Indian Ocean also varies across models (e.g., via ENSO–IOD coherence) and is thus a potential source for the conflicting results. As noted in section 5, a somewhat more subtle source of discrepancies
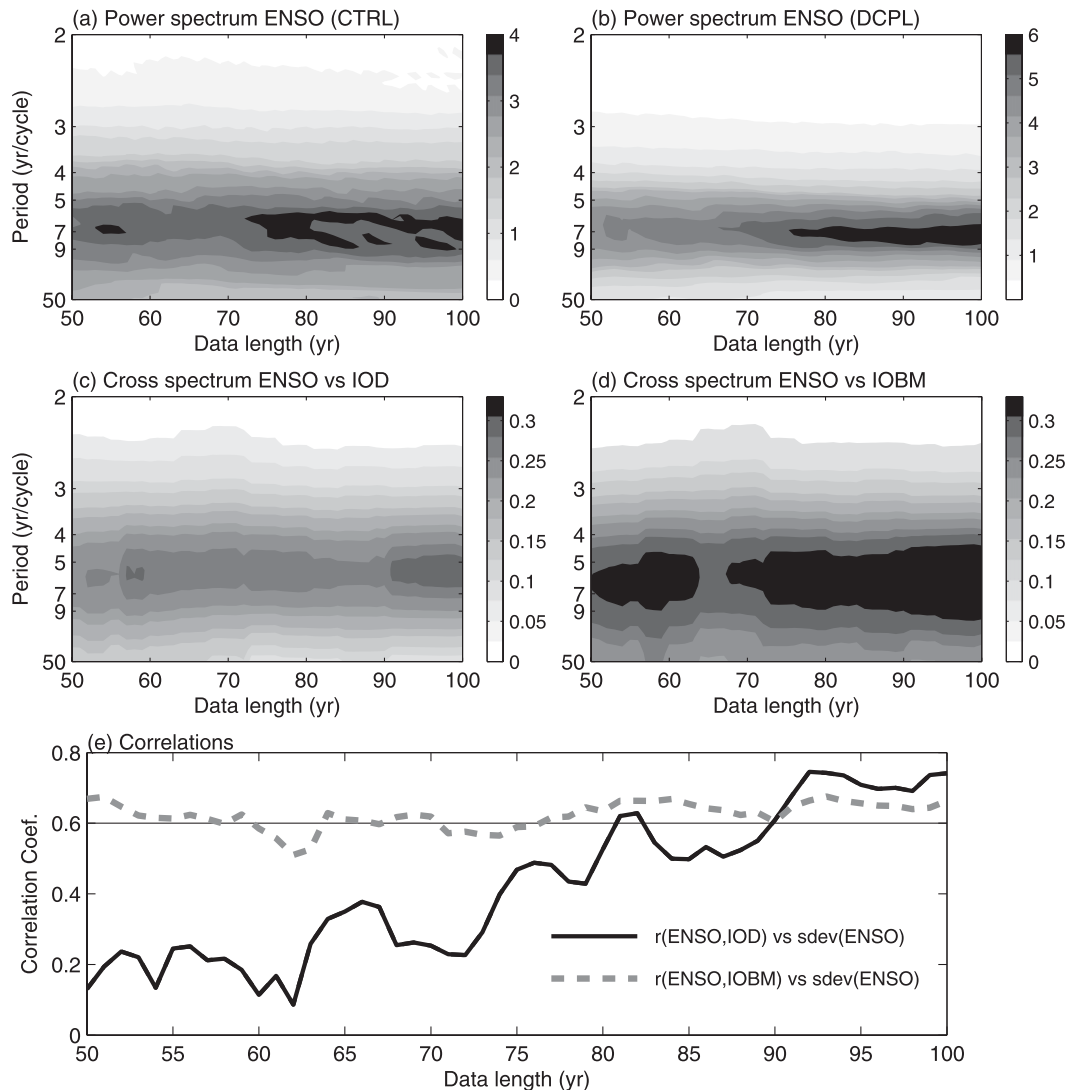
FIG. A1. (top) Power spectrum of ENSO characteristic time series in (a) CTRL and (b) DCPL as a function of data length, averaged over the 11 ensemble members. (middle) Amplitude of the cross spectra between (c) ENSO and IOD and (d) ENSO and IOBM in CTRL as a function of data length, averaged over the 11 ensemble members. (e) Correlations between the standard deviation of ENSO and the correlation between ENSO and IOD (ENSO and IOBM) across the 11 epochs in CTRL as a function of data length shown in thick black (thick dashed gray) line. The horizontal line indicates the 95% correlation significance level, which is calculated based on 11 samples for each data length. The ENSO, IOD, and IOBM time series are taken as the standardized principal components of the corresponding EOF modes shown in Fig. 2. In (e), the ENSO–IOBM correlation is based on the correlation between September–December ENSO and the following boreal winter–spring IOBM, which exhibits a high lag correlation as shown in Fig. 2i.

across the decoupling studies may be whether or not the Indonesian seas are included as part of the Pacific Ocean in the experiments. The role of the Indonesian seas within the context of this work will be investigated further in the future. Finally, as noted in the appendix, it is also necessary that the time series for analysis are reasonably long to sample the ENSO and Indian Ocean variability to avoid arriving in an erroneous conclusion.

Our study suggests that the IOBM acts as a damping mechanism for ENSO, with an influence on dynamical processes in the Pacific. Relative to the IOBM, the IOD is favorable for ENSO growth. Although the Indo-Pacific feedback interactions diagnosed in this study arise from a bias in the simulated ENSO that is of longer period than in recent observations, the mechanisms revealed here may be applicable for low-frequency modulation

of ENSO in the real system. Our study puts these feedback processes within the context of ENSO dynamics, suggesting the plausibility that the possible peculiar occurrences of the IOBM during the ENSO developing phase prior to 1976 or the lack of IOD thereof, as opposed to the more prevalent IOD post-1976, may be linked to the epochal shift in ENSO behavior. This is an interesting topic for further investigation. Overall, this study demonstrates that feedbacks from the Indian Ocean can significantly influence ENSO dynamics, thus supporting the notion that the Indian Ocean should be regarded as an integral component of ENSO, as demonstrated, for example, in the conceptual recharge oscillator model of Kug and Kang (2006) and Jansen et al. (2009).

APPENDIX

Variability Time Scales and Data Record Length

The ENSO period in the model is rather long compared with that observed (5–9 yr; see section 3), which slightly increases in DCPL (Fig. 5c). It is thus necessary that the length of the time series used for the analysis is reasonably long to resolve ENSO variability and its relationship with the IOD and IOBM. The intensifying ENSO spectra and ENSO–IOD cross spectra with increasing data record length (Figs. A1a–c) suggest that time series longer than 90 yr appear to better capture the model's ENSO variability and its relationship with the IOD.

Significant correlations between ENSO magnitude and ENSO–IOD coherence across the 11 epochs in CTRL also start to emerge when the data record is longer than 90 yr (Fig. A1e). The positive correlation stems from the fact that strong ENSO conditions can initiate IOD events. Such a mechanistic relationship also exists for the IOBM but does not appear to be as dependent on the length of data employed (see also
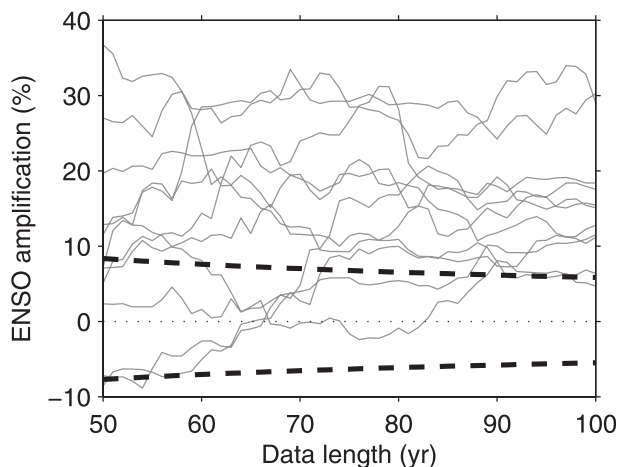

FIG. A2. Percentage changes in Niño-3.4 standard deviation in DCPL relative to CTRL as a function of data length for all corresponding 11 ensemble members (gray lines). Thick black dashed lines indicate the 95% confidence interval evaluated based on an F test for a null hypothesis for which the changes are not different from 0.

Fig. A1d). This is likely because the IOBM is largely a response to ENSO, whereas the IOD can often occur independently of ENSO (see section 3). This suggests that the ENSO variability and its covariation with the Indian Ocean variability, particularly the IOD, are likely to be better resolved with time series greater than 90 yr.

For the above reason, the analysis in this study is based on ensemble epochs that are 100 yr long. Therefore, the decoupling experiments are run for 100 yr each. As shown in Fig. 5b, the ENSO variability in DCPL relative to CTRL is consistently enhanced across the 11 ensemble members. However, when using shorter data lengths, the ENSO magnitude in DCPL may appear to weaken, although this is not statistically different from that in CTRL under an F test, as demonstrated in Fig. A2. However, as the spectral analysis above suggests, this is potentially due to undersampling of the ENSO variability.

REFERENCES

Annamalai, H., R. Murtugudde, J. Potemra, S. P. Xie, P. Liu, and B. Wang, 2003: Coupled dynamics over the Indian Ocean: Spring initiation of the zonal mode. *Deep Sea Res. II,* **50,** 2305–2330.

——, S. P. Xie, J. P. McCreary, and R. Murtugudde, 2005: Impact of Indian Ocean sea surface temperature on developing El Niño. *J. Climate,* **18,** 302–319.

——, S. Kida, and J. Hafner, 2010: Potential impact of the tropical Indian Ocean–Indonesian Seas on El Niño characteristics. *J. Climate,* **23,** 3933–3952.

Ashok, K., Z. Guan, and T. Yamagata, 2001: Impact of the Indian Ocean dipole on the relationship between the Indian monsoon rainfall and ENSO. *Geophys. Res. Lett.,* **28,** 4499–4502.

Behera, S. K., J. J. Luo, S. Masson, S. A. Rao, H. Sakuma, and T. Yamagata, 2006: A CGCM study on the interaction between IOD and ENSO. *J. Climate,* **19,** 1688–1705.

Cai, W., H. H. Hendon, and G. Meyers, 2005: Indian Ocean dipolelike variability in the CSIRO Mark 3 coupled climate model. *J. Climate,* **18,** 1449–1468.

——, A. Sullivan, and T. Cowan, 2009: Rainfall teleconnections with Indo-Pacific variability in the WCRP CMIP3 models. *J. Climate,* **22,** 5046–5071.

——, ——, and ——, 2011a: Interactions of ENSO, the IOD, and the SAM in CMIP3 models. *J. Climate,* **24,** 1688–1704.

——, P. van Rensch, T. Cowan, and H. H. Hendon, 2011b: Teleconnection pathways of ENSO and the IOD and the mechanisms for impacts on Australian rainfall. *J. Climate,* **24,** 3910–3923.

Dommenget, D., V. Semenov, and M. Latif, 2006: Impacts of the tropical Indian and Atlantic Oceans on ENSO. *Geophys. Res. Lett.,* **33,** L11701, doi:10.1029/2006GL025871.

Du, Y., S.-P. Xie, G. Huang, and K. Hu, 2009: Role of air–sea interaction in the long persistence of El Niño–induced North Indian Ocean warming. *J. Climate,* **22,** 2023–2038.

Fedorov, A. V., and S. G. Philander, 2001: A stability analysis of tropical ocean–atmosphere interactions: Bridging measurements and theory for El Niño. *J. Climate,* **14,** 3086–3101.

Fischer, A., P. Terray, E. Guilyardi, S. Gualdi, and P. Delecluse, 2005: Two independent triggers for the Indian Ocean dipole/zonal mode in a coupled GCM. *J. Climate,* **18,** 3428–3449.

Frauen, C., and D. Dommenget, 2012: Influences of the tropical Indian and Atlantic Oceans on the predictability of ENSO. *Geophys. Res. Lett.,* **39,** L02706, doi:10.1029/2011GL050520.

Guilyardi, E., 2006: El Niño-mean state-seasonal cycle interactions in a multi-model ensemble. *Climate Dyn.,* **26,** 329–348.

——, A. Wittenberg, A. Fedorov, M. Collins, C. Wang, A. Capotondi, G. J. van Oldenborgh, and T. Stockdale, 2009: Understanding El Niño in ocean–atmosphere general circulation models: Progress and challenges. *Bull. Amer. Meteor. Soc.,* **90,** 325–340.

Izumo, T., and Coauthors, 2010: Influence of the state of the Indian Ocean dipole on the following year's El Niño. *Nat. Geosci.,* **3,** 168–172.

Jansen, M. F., D. Dommenget, and N. Keenlyside, 2009: Tropical atmosphere–ocean interactions in a conceptual framework. *J. Climate,* **22,** 550–567.

Jin, F.-F., 1997: An equatorial ocean recharge paradigm for ENSO. Part I: Conceptual model. *J. Atmos. Sci.,* **54,** 811–829.

——, S. T. Kim, and L. Bejarano, 2006: A coupled-stability index for ENSO. *Geophys. Res. Lett.,* **33,** L23708, doi:10.1029/2006GL027221.

Kim, S. T., and F.-F. Jin, 2011: ENSO stability analysis. Part II: Results from the twentieth and twenty-first century simulations of the CMIP3 models. *Climate Dyn.,* **36,** 1609–1627.

Kirtman, B., and G. A. Vecchi, 2011: Why climate modelers should worry about atmospheric and oceanic weather. *The Global Monsoon System: Research and Forecast,* 2nd ed., C.-P. Chang et al., Eds., World Scientific, 511–523.

Klein, S. A., B. J. Soden, and N. C. Lau, 1999: Remote sea surface temperature variations during ENSO: Evidence for a tropical atmospheric bridge. *J. Climate,* **12,** 917–932.

Kug, J.-S., and I.-S. Kang, 2006: Interactive feedback between ENSO and the Indian Ocean. *J. Climate,* **19,** 1784–1801.

——, T. Li, S.-I. An, I.-S. Kang, J.-J. Luo, S. Masson, and T. Yamagata, 2006: Role of the ENSO–Indian Ocean coupling on ENSO variability in a coupled GCM. *Geophys. Res. Lett.,* **33,** L09710, doi:10.1029/2005GL024916.

Lau, N.-C., and M. J. Nath, 2003: Atmosphere–ocean variations in the Indo-Pacific sector during ENSO episodes. *J. Climate,* **16,** 3–20.

Liu, L., W. Yu, and T. Li, 2011: Dynamic and thermodynamic air–sea coupling associated with the Indian Ocean dipole diagnosed from 23 WCRP CMIP3 models. *J. Climate,* **24,** 4941–4958.

Luo, J.-J., S. Masson, E. Roeckner, G. Madec, and T. Yamagata, 2005: Reducing climatology bias in an ocean–atmosphere CGCM with improved coupling physics. *J. Climate,* **18,** 2344–2360.

——, R. Zhang, S. K. Behera, Y. Masumoto, F.-F. Jin, R. Lukas, and T. Yamagata, 2010: Interaction between El Niño and extreme Indian Ocean dipole. *J. Climate,* **23,** 726–742.

McPhaden, M. J., and X. Zhang, 2009: Asymmetry in zonal phase propagation of ENSO sea surface temperature anomalies. *Geophys. Res. Lett.,* **36,** L13703, doi:10.1029/2009GL038774.

Neelin, J. D., D. S. Battisti, A. C. Hirst, F.-F. Jin, Y. Wakata, T. Yamagata, and S. E. Zebiak, 1998: ENSO theory. *J. Geophys. Res.,* **103** (C7), 14 261–14 290.

Ohba, M., and H. Ueda, 2007: An impact of SST anomalies in the Indian Ocean in acceleration of the El Niño to La Niña transition. *J. Meteor. Soc. Japan,* **85,** 335–348.

Okumura, Y. M., and C. Deser, 2010: Asymmetry in the duration of El Niño and La Niña. *J. Climate,* **23,** 5826–5843.

Percival, D. B., and A. T. Walden, 1993: *Spectral Analysis for Physical Applications: Multitaper and Conventional Univariate Techniques.* Cambridge University Press, 583 pp.

Phipps, S. J., 2010: The CSIRO Mk3L climate system model v1.2. Antarctic Climate and Ecosystems Cooperative Research Centre Tech. Rep., Hobart, TAS, Australia, 121 pp.

Rayner, N. A., P. Brohan, D. E. Parker, C. K. Folland, J. J. Kennedy, M. Vanicek, T. Ansell, and S. F. B. Tett, 2006: Improved analyses of changes and uncertainties in sea surface temperature measured in situ since the mid-nineteenth century: The HadSST2 dataset. *J. Climate,* **19,** 446–469.

Saji, N. H., and T. Yamagata, 2003: Structure of SST and surface wind variability during Indian Ocean dipole mode events: COADS observations. *J. Climate,* **16,** 2735–2751.

——, B. N. Goswami, P. N. Vinayachandran, and T. Yamagata, 1999: A dipole mode in the tropical Indian Ocean. *Nature,* **401,** 360–363.

——, S.-P. Xie, and T. Yamagata, 2006: Tropical Indian Ocean variability in the IPCC twentieth-century climate simulations. *J. Climate,* **19,** 4397–4417.

Santoso, A., A. Sen Gupta, and M. H. England, 2010: Genesis of Indian Ocean mixed layer temperature anomalies: A heat budget analysis. *J. Climate,* **23,** 5375–5403.

——, W. Cai, M. H. England, and S. J. Phipps, 2011: The role of the Indonesian Throughflow on ENSO dynamics in a coupled climate model. *J. Climate,* **24,** 585–601.

Smith, T. M., R. W. Reynolds, T. C. Peterson, and J. Lawrimore, 2008: Improvements to NOAA's historical merged land–ocean surface temperature analysis (1880–2006). *J. Climate,* **21,** 2283–2296.

Taschetto, A. S., A. Sen Gupta, H. H. Hendon, C. C. Ummenhofer, and M. H. England, 2011: The contribution of Indian Ocean sea surface temperature anomalies on Australian summer rainfall during El Niño events. *J. Climate,* **24,** 3734–3747.

Wang, B., R. Wu, and R. Lukas, 1999: Roles of the western North Pacific wind variation in thermocline adjustment and ENSO phase transition. *J. Meteor. Soc. Japan,* **77,** 1–16.

Wang, C., W. Wang, D. Wang, and Q. Wang, 2006: Interannual variability of the South China Sea associated with El Niño. *J. Geophys. Res.,* **111,** C03023, doi:10.1029/2005JC003333.

Watanabe, M., and F.-F. Jin, 2002: Role of Indian Ocean warming in the development of Phillipine Sea anticyclone during ENSO. *Geophys. Res. Lett.,* **29,** 1478, doi:10.1029/2001GL014318.

Weisberg, R. H., and C. Wang, 1997: A western Pacific oscillator paradigm for the El Niño–Southern Oscillation. *Geophys. Res. Lett.,* **24,** 779–782.

Wittenberg, A. T., 2009: Are historical records sufficient to constrain ENSO simulations? *Geophys. Res. Lett.,* **36,** L12702, doi:10.1029/2009GL038710.

Wu, R., and B. P. Kirtman, 2004: Understanding the impacts of the Indian Ocean on ENSO variability in a coupled GCM. *J. Climate,* **17,** 4019–4031.

Yang, J., Q. Liu, S.-P. Xie, Z. Liu, and L. Wu, 2007: Impact of the Indian Ocean SST basin mode on the Asian summer monsoon. *Geophys. Res. Lett.,* **34,** L02708, doi:10.1029/2006GL028571.

Yu, J.-Y., C. R. Mechoso, J. C. McWilliams, and A. Arakawa, 2002: Impacts of the Indian Ocean on the ENSO cycle. *Geophys. Res. Lett.,* **29,** 1204, doi:10.1029/2001GL014098.

——, F. Sun, and H.-Y. Kao, 2009: Contributions of Indian Ocean and monsoon biases to the excessive biennial ENSO in CCSM3. *J. Climate,* **22,** 1850–1858.